Received June 28, 2021, accepted July 13, 2021, date of publication July 15, 2021, date of current version July 26, 2021.
Digital Object Identifier 10.1109/ACCESS.2021.3097633

Analysis and Optimization of 5G Coverage Predictions Using a Beamforming Antenna Model and Real Drive Test Measurements

MARCO SOUSA[1,2,3], ANDRÉ ALVES[2], PEDRO VIEIRA[1,4], MARIA PAULA QUELUZ[1,2], AND ANTÓNIO RODRIGUES[1,2], (Member, IEEE)
[1]Instituto de Telecomunicações, 1049-001 Lisboa, Portugal
[2]Departamento de Engenharia Electrotécnica e de Computadores, Instituto Superior Técnico, 1049-001 Lisboa, Portugal
[3]Celfinet—Outstanding Networks, 1495-764 Lisbon, Portugal
[4]Departamento de Engenharia Electrónica e Telecomunicações e de Computadores, Instituto Superior de Engenharia de Lisboa, 1959-007 Lisboa, Portugal
Corresponding author: Marco Sousa (marco.sousa@celfinet.com)

This work was supported by the COMPETE/Fundo Europeu de Desenvolvimento Regional (FEDER) through the Project AI4GREEN 16/SI/2019—I&DT Empresarial (Projetos Copromoção) and the International Project CELTIC-NEXT/EUREKA under Grant C2018/1-5.

ABSTRACT The ability to estimate radio coverage accurately is fundamental for planning and optimizing any wireless network, notably when a new generation, as the 5^{th} Generation (5G), is in an early deployment phase. The knowledge acquired from radio planning of previous generations must be revisited, particularly the used path loss and antennas models, as the 5G propagation is intrinsically distinct. This paper analyses a new beamforming antenna model and distinct path loss models - 3^{rd} Generation Partnership Project (3GPP) and Millimetre-Wave Based Mobile Radio Access Network for Fifth Generation Integrated Communications (mmMAGIC) - applying them to evaluate 5G coverage in 3-Dimensional (3D) synthetic and real scenarios, for outdoor and indoor environments. Further, real 5G Drive Tests (DTs) were used to evaluate the 3GPP path loss model accuracy in Urban Macro (UMa) scenarios. For the new antenna model, it is shown that the use of beamforming with multiple vertical beams is advantageous when the Base Station (BS) is placed below the surrounding buildings; in regular UMa surroundings, one vertical beam provides adequate indoor coverage and a maximized outdoor coverage after antenna tilt optimization. The 3GPP path loss model exhibited a Mean Absolute Error (MAE) of 21.05 dB for Line-of-Sight (LoS) and 14.48 dB for Non-Line-of-Sight (NLoS), compared with real measurements. After calibration, the MAE for LoS and NLoS decreased to 5.45 dB and 7.51 dB, respectively. Moreover, the non-calibrated 3GPP path loss model led to overestimations of the 5G coverage and user throughput up to 25% and 163%, respectively, when compared to the calibrated model predictions. The use of Machine Learning (ML) algorithms resulted in path loss MAEs within the range of 4.58 dB to 5.38 dB, for LoS, and within the range of 3.70 dB to 5.96 dB, for NLoS, with the Random Forest (RF) algorithm attaining the lowest error.

INDEX TERMS 5G, mmWaves, 3D propagation, path loss models, antenna models, beamforming, calibration, machine learning.

I. INTRODUCTION

The evolution of Mobile Wireless Networks (MWN), progressing from 4^{th} Generation (4G) to 5G networks, has introduced new technologies, new concepts, and even new frequency bands. From the radio coverage perspective, both Millimeter Waves (mmWaves) and Massive Multiple-Input Multiple-Output (mMIMO) will be two of the most impactful technologies. Among other drivers, the subject of radio propagation and channel modeling has become a hot research topic for 5G, since it unlocks the fundamentals for planning 5G deployments, notably 5G coverage and interference optimization.

The 5G radio network planning and optimization require proper large-scale coverage prediction, adopting reliable antenna gain and path loss models; even though both models can be unified into one as in [1] or [2], the standard approach is to consider them separately.

The associate editor coordinating the review of this manuscript and approving it for publication was Franco Fuschini.

As for the antenna gain models, with beamforming support, current approaches are mainly of two types. The first considers the antenna gain as a result of the product between the antenna array factor (modeling directivity), and the antenna element radiation pattern. The second simplifies the radiation pattern (*e.g.,* to a flat-top antenna pattern) quantifying the antenna array gains in a binary manner, according to the width of beams. Whereas the former is more realistic, it requires information about the physical properties of the antenna arrays; the latter is less accurate, but easily implemented [3]–[5].

Concerning large-scale path loss models, these are usually classified as stochastic or deterministic. Deterministic models rely on electromagnetic fundamentals (*e.g.,* Maxwell equations) to predict path loss, while stochastic models consider probability distributions for the radio channel parameters, obtained from extensive DT campaigns. The deterministic models are more accurate than other modeling approaches. However, they have high computational complexity and require precise environment information. On the contrary, models obtained by the stochastic approach are mathematically tractable but less accurate [6]. In coverage predictions of large areas, the stochastic models are preferred due to their computational efficiency.

This work has three main objectives: to evaluate 5G coverage predictions using current stochastic path loss and antenna models, in distinct propagation scenarios and antenna beamforming configurations; to measure the path loss prediction accuracy of current models; to increase the path loss prediction accuracy, and assess the resulting 5G coverage.

The main contributions of this paper are summarized as follows:

- An extended and more detailed analysis of the beamforming antenna model, proposed by the authors in [7], is performed including a new comparison with a single beam antenna model.
- A detailed comparison, using two synthetic scenarios, between the path loss predictions of the 3GPP TR 38.901, and the mmMAGIC models is provided, considering the effects of existing (or not) LoS, distinct antenna radiation patterns, and different frequencies.
- An analysis of 5G coverage in real scenarios, using high resolution 3D data and real Mobile Network Operator (MNO) information, evaluating coverage impacts of distinct building geometries. The 5G coverage analysis includes also a detailed analysis of indoor coverage for different antenna configurations.
- The assessment of the 3GPP TR 38.901 path loss model accuracy is achieved considering real 5G DT campaigns, with and without model calibration.
- The development and assessment of calibrated path loss models for 5G coverage analysis is provided, based on received power-dependent metrics (*e.g.,* percentage of the covered area or throughput).
- A set of data-driven path loss models, based on ML regression algorithms over real 5G measurements are derived, and their accuracy assessed.

This paper is organized as follows. After the introduction provided in Section I, Section II presents the fundamental concepts underlying this work and highlights related work. Section III gives a brief description of the beamforming antenna model that will be considered for the rest of the paper and compares it with a single beam 3GPP antenna model. In Section IV, the considered path loss models - 3GPP TR 38.901 and mmMAGIC - are overviewed. In section V, the 5G coverage metrics to be used in several scenarios are presented. Section VI aims to evaluate 5G coverage, considering a set of synthetic and real propagation scenarios, where distinct antenna radiation patterns, carrier frequencies, and network deployment types are assessed. In Section VII, DT data is first used to quantify the prediction error of the considered path loss model. This model is then calibrated with the DT path loss measurements, and the resulting improvement of the path loss prediction is evaluated. Finally, the DT data is used with ML algorithms to develop data-driven path loss models, that are compared with the standard path loss approaches. Section VIII presents the main conclusions and final remarks.

II. BACKGROUND AND RELATED WORK

The field of radio propagation and channel modeling, particularly under the 5G framework and standards, has received lots of attention and several new contributions. These are summarized in [8], where the authors evaluate the main 5G propagation challenges, outline solutions and directions for the 5G usage scenarios. One of the greatest radio coverage challenges towards 5G is created by the use of mmWaves. Extensive overviews on this subject are presented in [9]–[11].

The use of mmWaves frequency bands causes severe signal attenuation being the signal also more susceptible to blockage and scattering. A way forward to increase coverage, at these higher frequencies, is to employ mMIMO antennas and use the higher gain of beamforming patterns.

Several architectures are proposed for beamforming antennas, from analog to fully digital, and even hybrid. Hybrid architectures achieve the best compromise between hardware/cost and performance, thus are the most used [12]. For all architectures, linear array antenna theory still applies to derive an approximation of the antenna radiation pattern, F, according to:

$$F(\theta, \phi) = F_{element}(\theta, \phi) \times AF_{array}(\theta, \phi) \tag{1}$$

where θ and ϕ are the vertical and horizontal angles, $F_{element}$ is the array element radiation pattern, and AF_{array} is the array factor that controls the directivity of the beams [13]. The array factor also depends on the signal wavelength, on the spacing between antenna elements and their total number, and on the signal phase in each antenna element. In [14], the authors provide an overview of the design of antenna arrays for mmWave communications, including the array parameters.

5G radio planning is generally conducted using stochastic path loss models, from which two primary variants are considered: the Alpha-Beta-Gamma (ABG) and the Close In (CI) models; both are frequency generic and can be also applied to mmWave. The ABG model, also known as Floating Intercept (FI) model, is given by [15]:

$$PL^{ABG}(f, d) = 10\alpha \log_{10}\left(\frac{d_{3D}}{1\ m}\right) + \beta + 10\gamma \log_{10}\left(\frac{f}{1\ GHz}\right) + \chi_\sigma^{ABG} \quad (2)$$

where α and γ are coefficients denoting the dependence of path loss on distance and frequency, respectively, whereas β is an optimized offset value. The variable d_{3D} is the 3D distance between the Transmitter (TX) and the Receiver (RX) in meters, f is the carrier frequency in GHz, and χ_σ^{ABG} is the Shadow Fading (SF) standard deviation. The coefficients α, β and γ are obtained directly from real signal measurement campaigns, fitting to the measured data.

The CI model is given by [15]:

$$PL^{CI}(f, d) = FSPL(f, 1\ m) + 10n \log_{10}(d_{3D}) + \chi_\sigma^{CI} \quad (3)$$

where n denotes the only parameter of the model, known as Path Loss Exponent (PLE), FSPL(f,1 m) is the Free Space Path Loss (FSPL) at a TX, RX separation of 1 m and carrier frequency f, and χ_σ^{CI} is the SF standard deviation.

Results in [15] and [16] show that both the CI and the ABG models exhibit similar performance when calibrated with real DT measurements. However, when extrapolating to frequencies outside the data used to fit the model, the CI model is preferable due to its simplicity and higher stability.

Several 5G stochastic path loss models have been developed, such as the 3GPP TR 38.901 [17], the NYUSIM [18], and the mmMAGIC [19]. While both the 3GPP TR 38.901 and the mmMAGIC are ABG based models, the NYUSIM path loss model is based on the CI variant. Deterministic models, as the Mobile and Wireless Communications Enablers for Twenty-twenty Information Society (METIS) [20] and the IEEE 802.11ad [21] have also been proposed, as well as semi-deterministic models, which use a hybrid approach between stochastic and deterministic, as the Millimetre-Wave Evolution for Backhaul and Access (MiWEBA) [22].

Additionally, with a broad range of 5G applications and services, several 5G coverage analyses have been carried out evaluating its technical feasibility. In [23], the authors evaluate the coexistence of dedicated indoor and outdoor radio coverage solutions, in a synthetic scenario, for mmWave communications. The use of synthetic scenarios has also been explored by the authors in [7]. In [23], a real scenario was considered where the feasibility of reusing 4G legacy sites for 3.5 GHz 5G networks was evaluated. The 5G coverage analyses are mainly supported by path loss models, and even though that most of the used path loss models were developed through extensive measurements campaigns, these campaigns have their specificity regarding the propagation environment, used frequencies, etc.; further measurements, in additional transmission conditions, are required to evaluate the models' accuracy and support the coverage analysis results. In [24], the authors evaluated, with real measurements, three candidate path loss models for the use over the entire 5G microwave and mmWave radio spectrum: the ABG, the CI, and the Close In Frequency (CIF). The authors concluded that the three models are comparable in prediction accuracy for large data sets. In [25], the authors verified a Root Mean Square Error (RMSE) of 10.32 dB between the measured path loss and the 3GPP UMa path loss predictions using a carrier frequency of 27.1 GHz. However, the path loss accuracy was only evaluated considering 14 distinct measurement locations.

Finally, there is a recent trend in using ML algorithms to develop data-driven path loss models from real measurements. In [26], the authors applied Artificial Neural Networks (ANNs) to predict the path loss achieving a mean error of 0 dB and a maximum error of 22 dB compared with the real measurements. The authors studied signal measurements using a frequency of 881.52 MHz in a rural open area. Additionally, the average received signal power was computed by averaging signal measurements over a measurement track of 300 wavelengths. Also, in [27], the use of ANNs achieved a MAE of 4.74 dB considering a carrier frequency of 1.8 GHz and radio measurements from 11 BSs. In [28], a Deep Neural Network (DNN) was used to predict path loss with a RMSE of 4 dB. However, the radio measurements were limited to an university campus and used 4G as radio technology. Nonetheless, it remains challenging to guarantee that sufficient generalization is achieved when considering ML-based models [29].

III. ANTENNA MODELS

This section starts by presenting the standard 3GPP antenna model [17], which is a single beam model for both the horizontal and vertical planes. Next, a new antenna model, recently proposed by the authors in [7] that enables multiple beams in horizontal and vertical planes, is described. Finally, a brief comparison between the two antenna models is presented.

A. 3GPP ANTENNA MODEL

The horizontal radiation pattern of the 3GPP model is given by:

$$A_H(\phi) = -\min\left\{12\left(\frac{\phi - \phi_{az}}{\phi_{-3dB}}\right)^2, A_m\right\} \quad (4)$$

where ϕ ($\in [-180°, 180°]$) is the horizontal angle measured between the BS boresight and the line in the horizontal plane connecting the User Equipment (UE) to the BS, ϕ_{az} denotes the fixed orientation angle of the BS boresight, ϕ_{-3dB} is the horizontal Half-Power Beamwidth (HPBW), and A_m is the maximum horizontal attenuation. The horizontal radiation pattern is also presented in Fig. 1.

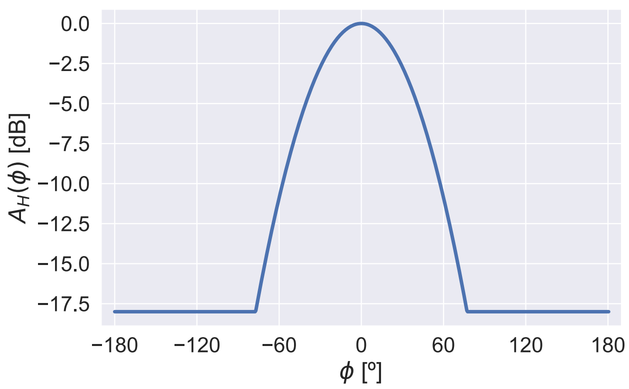

FIGURE 1. Horizontal radiation pattern of the 3GPP antenna model ($\phi_{az} = 0°$; $\phi_{-3dB} = 63°$; $A_m = 18$ dB).

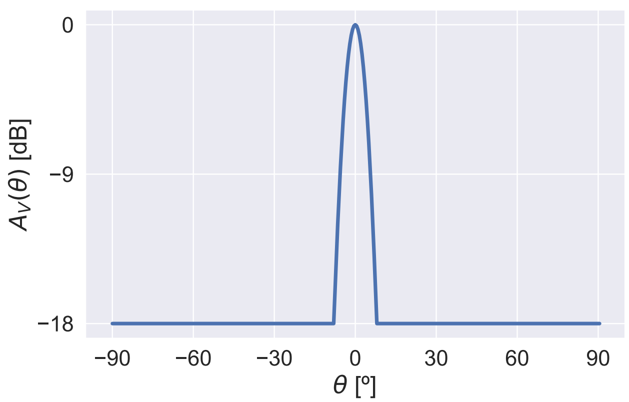

FIGURE 2. Vertical radiation pattern of the 3GPP antenna model ($\theta_{tilt} = 0°$; $\theta_{-3dB} = 6.5°$; $A_m = 18$ dB).

Similarly, the vertical radiation pattern is given by:

$$A_V(\theta) = -\min\left\{12\left(\frac{\theta - \theta_{tilt}}{\theta_{-3dB}}\right)^2, \text{SLL}\right\} \tag{5}$$

where θ ($\in [-90°, 90°]$) is the vertical angle measured between the horizon and the line connecting the UE to the BS, θ_{tilt} denotes the antenna tilt and is measured between the horizon and the line passing through the peak of the beam, θ_{-3dB} is the vertical HPBW, and SLL is the vertical Side-Lobe Level (SLL). The vertical radiation pattern is depicted in Fig. 2.

Finally, the 3D antenna gain is obtained as:

$$G_{3D}(\theta, \phi) = G_m - \min\{-[A_H(\phi) + A_V(\theta)], A_m\} \tag{6}$$

where G_{m} denotes the peak antenna gain in dBi. The 3D representation of the 3GPP antenna gain is presented in Fig. 3.

B. BEAMFORMING ANTENNA MODEL

One of the main features of 5G is mMIMO antennas, which allow beamforming. By forming extremely accurate user-level narrow beams, signal coverage is improved, and interference between cells is reduced [30]. This section describes a new approach in antenna modeling that models 5G Active Antenna Systems (AASs) with beamforming.

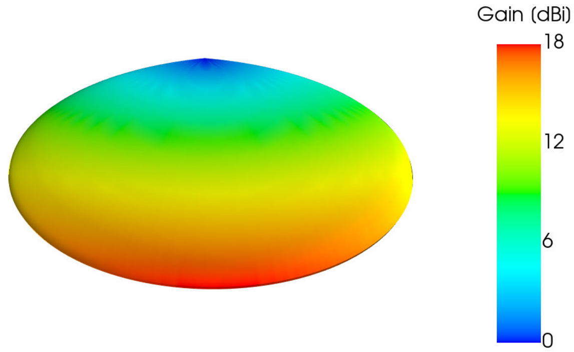

FIGURE 3. 3D radiation pattern of the 3GPP antenna model ($G_m = 18$ dBi).

The horizontal radiation pattern, of the beamforming antenna model, is defined by:

$$A_H(\phi) = -\min\left\{12\left(\frac{\phi - k_H(\phi)}{\phi_{-3dB}}\right)^2, A_m\right\} \tag{7}$$

where $k_H(\phi)$ is the offset angle for the horizontal beam covering direction, ϕ:

$$k_H(\phi) = min_{\text{range},H} + \phi_{A_{\text{beam}}}\left(\frac{1}{2} + i(\phi)\right) \tag{8}$$

where $min_{\text{range},H}$ is the lower limit of the antenna horizontal scanning range, $\phi_{A_{\text{beam}}}$ is a constant and $i(\phi)$ identifies the used beam in the ϕ direction. The factor $\phi_{A_{\text{beam}}}$ is given by:

$$\phi_{A_{\text{beam}}} = \frac{max_{\text{range},H} - min_{\text{range},H}}{n_H} \tag{9}$$

where $max_{\text{range},H}$ is the higher limit of the antenna horizontal scanning range and n_H is the number of horizontal beams.

The function $i(\phi)$, which identifies the beam covering direction ϕ, is given by:

$$i(\phi) = \min\left\{\left\lfloor\frac{\max(\phi - min_{\text{range},H}, 0)}{\phi_{A_{\text{beam}}}}\right\rfloor, n_H - 1\right\} \tag{10}$$

Similarly, the vertical radiation pattern is obtained as follows:

$$A_V(\theta) = -\min\left\{12\left(\frac{\theta - k_V(\theta)}{\theta_{-3dB}}\right)^2, \text{SLL}\right\} \tag{11}$$

where $k_V(\theta)$ is the offset angle for the vertical beam covering direction, θ:

$$k_V(\theta) = min_{\text{range},V} + \theta_{A_{\text{beam}}}\left(\frac{1}{2} + j(\theta)\right) \tag{12}$$

where $min_{\text{range},V}$ is the inferior limit of the antenna vertical scanning range, $\theta_{A_{\text{beam}}}$ is a constant and $j(\theta)$ identifies the used beam in the θ direction. The factor $\theta_{A_{\text{beam}}}$ is defined as:

$$\theta_{A_{\text{beam}}} = \frac{max_{\text{range},V} - min_{\text{range},V}}{n_V} \tag{13}$$

where $max_{\text{range},V}$ is the superior limit of the antenna vertical scanning range and n_V is the number of vertical beams.

The function $j(\theta)$, which identifies the beam covering direction θ, is given by:

$$j(\theta) = \min\left\{\left\lfloor \frac{\max(\theta - min_{\text{range},V}, 0)}{\theta_{A_{\text{beam}}}} \right\rfloor, n_V - 1\right\} \quad (14)$$

The 3D antenna gain, G_{3D}, of the beamforming antenna model is obtained from (6).

Throughout this work, both antenna models were parameterized according to the datasheet of commercial antennas. The commercial antenna, Kathrein 742212, was used with the 3GPP antenna model, while the antenna Huawei AAU5613, which supports beamforming, was used with the beamforming antenna model. Additionally, the antenna AAU5613 has distinct radiation patterns that are also presented in Table 1.

TABLE 1. List of antenna configurations.

Antenna Pattern	Model	Hor. Beams	Vert. Beams	Hor. HPBW	Vert. HPBW
Kathrein	3GPP	1	1	63.0º	6.5º
Pattern 1	Beamforming	8	1	110.0º	6.0º
Pattern 6	Beamforming	8	1	110.0º	12.0º
Pattern 9	Beamforming	4	2	45.0º	12.0º
Pattern 15	Beamforming	2	4	25.0º	25.0º

Note that the columns for the HPBW, in the case of the beamforming model, correspond to the global radiation pattern and not to the beams individually. As an example, and considering the radiation pattern 9, the respective 3D gain using the beamforming model is displayed in Fig. 4.

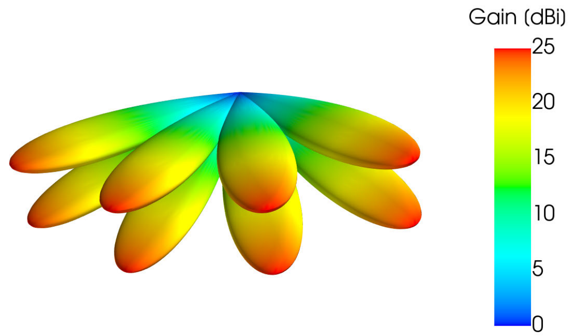

FIGURE 4. 3D radiation pattern of the beamforming antenna model with radiation pattern 9 (4 horizontal beams, 2 vertical beams).

It is worth noting that in legacy antennas with a single beam, the tilt direction coincides with the antenna maximum gain. However, when considering beamforming radiation patterns, with multiple vertical beams, (see Fig. 4 as an example), as on the vertical plane the maximum gain is not obtained for $\theta = 0°$, the tilt direction does not provide the maximum vertical antenna gain.

C. ANTENNA MODELS COMPARISON

In this section, the two antenna models (3GPP and beamforming) are compared, considering the radiation pattern 6 for the beamforming model and the Kathrein antenna for the 3GPP model. The parameters used in both models, are presented in Table 2.

TABLE 2. Antenna parameters for the comparison between the 3GPP and the beamforming models.

Parameter	Beamforming Model	3GPP Model
ϕ_{-3dB}	14 °	63 °
A_m	30 dB	25 dB
Horizontal Range	-60 ° to 60 °	-
n_H	8	1
θ_{-3dB}	6 °	6.5 °
SLL	18 dB	18 dB
Vertical Range	-15 ° to 15 °	-
n_V	1	1
G_m	25 dBi	18 dBi

A simplified scenario, to study the antenna 3D gain of the beamforming antenna model, is presented in Fig. 5 for the horizontal plane.

The scenario has the following specifications: an area of 1 km × 1 km; a 3-sector BS at the center with an antenna height of 25 m; a UE height of 1.5 m; and antenna tilt such that the vertical gain in the horizon direction is 6 dB below the maximum.

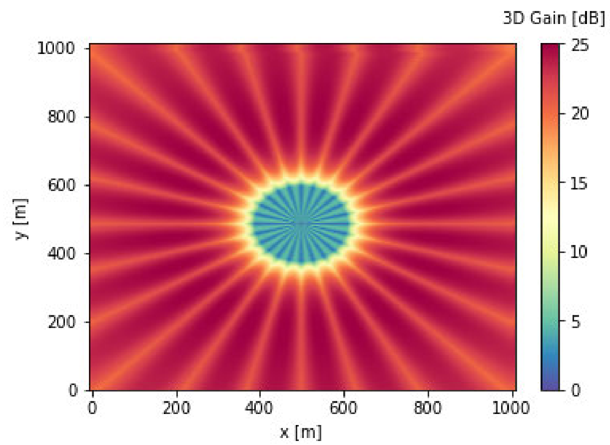

FIGURE 5. 3D gain of a beamforming antenna in the horizontal plane, at a height of 1.5 m (top view).

Fig. 5 exhibits the influence of the horizontal beams (eight by sector) while Fig. 6 exhibits the antenna model gain distribution on the vertical plane (with a single vertical beam).

To compare both antenna models, and evaluate the impact of adopting beamforming, the 3D gain difference, in the reference scenario, is represented in Fig. 7.

The beamforming antenna model has a 3D gain improvement, relatively to the classical single beam radiation pattern, that ranges from 0 dB to 16 dB, and is particularly relevant in the areas between sectors. As can be concluded from Fig. 7, with beamforming, radio coverage is no longer sector-based (or cell-based) but beam-based.

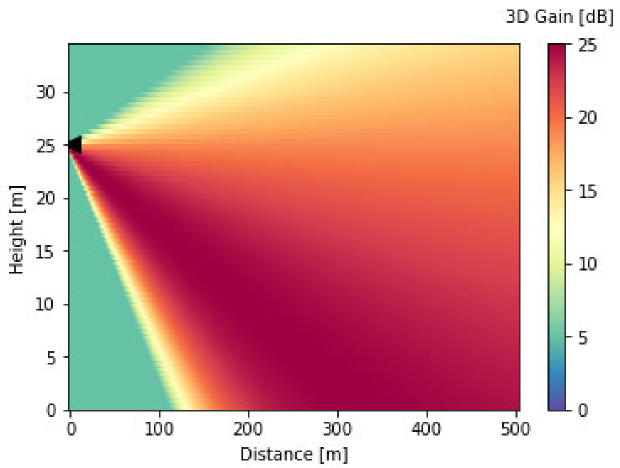

FIGURE 6. 3D gain of a beamforming antenna in the vertical plane, at an azimuth of 7.5° (side view).

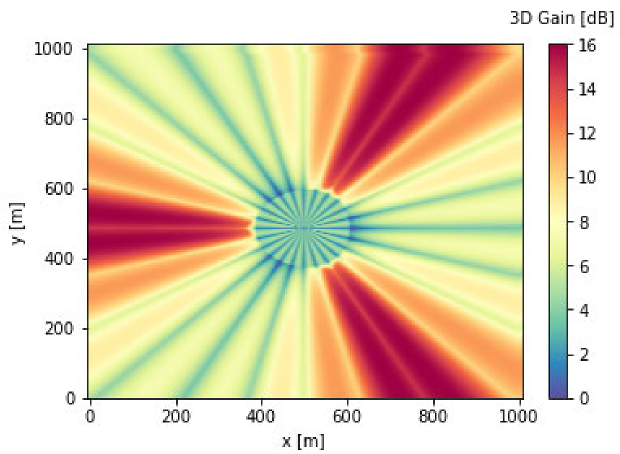

FIGURE 7. 3D gain difference between the beamforming and the 3GPP model, in the horizontal plane, at a height of 1.5 m (top view).

IV. 5G PATH LOSS MODELS

The 5G standard introduced new enhancements to support its services and use cases. Accordingly, the propagation modeling for 5G has been revised, considering new standards (*e.g.* new frequency bands, beamforming antennas), leading to new path loss models [8].

This section presents the two 5G path loss models considered in this paper, the 3GPP TR 38.901 and the mmMAGIC.

A. 3GPP TR 38.901 PATH LOSS MODEL

The current 3GPP path loss model, the 3GPP TR 38.901, was developed over previous existing models, admitting some of the new 5G propagation requirements. The latest version is valid for a wide range of carrier frequencies (f_c), from 0.5 GHz to 100 GHz, and a limited number of propagation scenarios [8].

Focusing on the urban environments, the 3GPP path loss model is valid for Urban Macro (UMa) and Urban Micro (UMi) deployments. For these, the respective path loss models for LoS links are dual-slope models, *i.e.*, they have different path loss functions depending on whether the 2-Dimensional (2D) distance between the BS and the UE, d_{2D}, is smaller than a breakpoint distance, d'_{BP}, or not (see Table 3). The breakpoint distance is defined as the distance from the BS to the point where the 1st Fresnel ellipsoid touches the terrain and where the Path Loss Exponent (PLE) shifts from free space (PLE = 2) to the asymptotic two-ray ground bounce model (PLE = 4) [31]. The LoS breakpoint distance, d'_{BP}, is given by:

$$d'_{\mathrm{BP}} = 4\frac{h'_{\mathrm{BS}}h'_{\mathrm{UE}}}{\lambda_c} \tag{15}$$

where h'_{BS} and h'_{UE} are the effective antenna heights at the BS and the UE locations, given by:

$$\begin{aligned} h'_{\mathrm{BS}} &= h_{\mathrm{BS}} + h_{\mathrm{geospatial,BS}} - h_{\mathrm{geospatial,UE}} \\ h'_{\mathrm{UE}} &= h_{\mathrm{UE}} \end{aligned} \tag{16}$$

where, h_{BS} and h_{UE} are the BS and UE height above terrain, $h_{\mathrm{geospatial,BS}}$ and $h_{\mathrm{geospatial,UE}}$ are, respectively, the BS and UE heights above sea level. In NLoS conditions, the 3GPP path loss model follows the ABG model, with an additional correction term for the UE height. The 3GPP UMi and UMa model parameters are presented in Table 3. Additionally, the 3GPP models consider a log-normal distribution for the SF, which is described by its standard deviation σ_{SF} (also in Table 3).

The 3GPP TR 38.901 [17] has an Outdoor-to-Indoor (O2I) penetration loss model, which is useful to describe the additional losses that an indoor UE may experience. Thereby, the path loss experienced by an indoor user is given by:

$$\mathrm{PL} = \mathrm{PL_b} + \mathrm{PL_{tw}} + \mathrm{PL_{in}} + \mathcal{N}(0, \sigma_P^2) \tag{17}$$

where $\mathrm{PL_b}$ is the outdoor path loss, $\mathrm{PL_{tw}}$ is the building penetration loss through the external wall, $\mathrm{PL_{in}}$ is the inside loss, dependent on the depth into the building, and $\mathcal{N}$ is a log-normal distribution, with zero mean and standard deviation, σ_P, for the penetration loss. The penetration loss is given by:

$$\mathrm{PL_{tw}} = \mathrm{PL_{npi}} + 10\log_{10}\sum_{i=1}^{N}\left(p_i \times 10^{-\frac{L_{\mathrm{material},i}}{10}}\right) \tag{18}$$

where $\mathrm{PL_{npi}}$ is an additional loss added to the external wall loss to account for non-perpendicular incidence, which is 5 dB in the 3GPP model, p_i is the proportion of the i-th material, under the condition that $\sum_{i=1}^{N} p_i = 1$, for all the N materials, and $L_{\mathrm{material},i}$ is the i-th material penetration loss. The material penetration loss is given by:

$$L_{\mathrm{material},i} = a_{\mathrm{material},i} + b_{\mathrm{material},i} \cdot f_c \tag{19}$$

where $\mathrm{a}_{\mathrm{material},i}$ and $\mathrm{b}_{\mathrm{material},i}$ are material dependent loss constants, and f_c is the frequency. Penetration loss of several materials may be found in [17].

TABLE 3. UMa and UMi path loss models.

Model		Path Loss (PL $[dB]$, f_c $[GHz]$, d $[m]$)	$\sigma_{SF}[dB]$	Applicability range and default values
3GPP UMa [17]	LoS	$\mathrm{PL}_{\text{UMa-LoS}} = \begin{cases} \mathrm{PL}_1 & \text{if } 10\text{ m} \le d_{2D} \le d'_{BP} \\ \mathrm{PL}_2 & \text{if } d'_{BP} < d_{2D} \le 5\text{ km} \end{cases}$ $\mathrm{PL}_1 = 28 + 22\log_{10}(d_{3D}) + 20\log_{10}(f_c)$ $\mathrm{PL}_2 = 28 + 40\log_{10}(d_{3D}) + 20\log_{10}(f_c) - 9\log_{10}((d'_{\text{BP}})^2 + (h_{\text{BS}} - h_{\text{UE}})^2)$	4	$0.5 < f_c < 100$ GHz $10 < d_{2D} < 5000$ m $1.5 \le h_{\text{UE}} \le 22.5$ m $h_{\text{BS}} = 25$ m
	NLoS	$\mathrm{PL}_{\text{UMa-NLoS}} = \max\left(\mathrm{PL}_{\text{UMa-LoS}}, \mathrm{PL}'_{\text{UMa-NLoS}}\right)$ $\mathrm{PL}'_{\text{UMa-NLoS}} = 13.54 + 39.08\log_{10}(d_{3D}) + 20\log_{10}(f_c) - 0.6\log_{10}(h_{\text{UE}} - 1.5)$	6	
3GPP UMi [17]	LoS	$\mathrm{PL}_{\text{UMi-LoS}} = \begin{cases} \mathrm{PL}_1 & \text{if } 10\text{ m} \le d_{2D} \le d'_{BP} \\ \mathrm{PL}_2 & \text{if } d'_{BP} < d_{2D} \le 5\text{ km} \end{cases}$ $\mathrm{PL}_1 = 32.4 + 21\log_{10}(d_{3D}) + 20\log_{10}(f_c)$ $\mathrm{PL}_2 = 32.4 + 40\log_{10}(d_{3D}) + 20\log_{10}(f_c) - 9.5\log_{10}((d'_{\text{BP}})^2 + (h_{\text{BS}} - h_{\text{UE}})^2)$	4	$0.5 < f_c < 100$ GHz $10 < d_{2D} < 5000$ m $1.5 \le h_{\text{UE}} \le 22.5$ m $h_{\text{BS}} = 10$ m
	NLoS	$\mathrm{PL}_{\text{UMi-NLoS}} = \max\left(\mathrm{PL}_{\text{UMi-LoS}}, \mathrm{PL}'_{\text{UMi-NLoS}}\right)$ $\mathrm{PL}'_{\text{UMi-NLoS}} = 22.4 + 35.3\log_{10}(d_{3D}) + 21.3\log_{10}(f_c) - 0.3\log_{10}(h_{\text{UE}} - 1.5)$	7.82	
3GPP Indoor [17]	LoS	$\mathrm{PL}_{\text{Ind-LoS}} = 32.4 + 17.3\log_{10}(d_{3D}) + 20\log_{10}(f_c)$	3	$0.5 < f_c < 100$ GHz $1\,m \le d_{3D} \le 150$ m
	NLoS	$\mathrm{PL}'_{\text{Ind-NLoS}} = 17.3 + 38.3\log_{10}(d_{3D}) + 24.9\log_{10}(f_c)$ $\mathrm{PL}_{\text{Ind-NLoS}} = \max\left(\mathrm{PL}_{\text{Ind-LoS}}, \mathrm{PL}'_{\text{Ind-NLoS}}\right)$	8.03	
mmMAGIC UMi [19]	LoS	$\mathrm{PL}_{\text{UMi-LoS}} = 32.9 + 19.2\log_{10}(d_{3D}) + 20.8\log_{10}(f_c)$	2	$6 < f_c < 100$ GHz $1.5 \le h_{\text{UE}} \le 3$ m $1.5 \le h_{\text{BS}} \le 10$ m
	NLoS	$\mathrm{PL}_{\text{UMi-NLoS}} = 31 + 45\log_{10}(d_{3D}) + 20\log_{10}(f_c)$	7.82	
mmMAGIC Indoor [19]	LoS	$\mathrm{PL}_{\text{Ind-LoS}} = 33.6 + 13.8\log_{10}(d_{3D}) + 20.3\log_{10}(f_c)$	1.18	$6 < f_c < 100$ GHz $1\text{ m} \le d_{3D} \le 150\text{ m}$
	NLoS	$\mathrm{PL}'_{\text{Ind-NLoS}} = 15.2 + 36.9\log_{10}(d_{3D}) + 26.8\log_{10}(f_c)$ $\mathrm{PL}_{\text{Ind-NLoS}} = \max\left(\mathrm{PL}_{\text{Ind-LoS}}, \mathrm{PL}'_{\text{Ind-NLoS}}\right)$	8.03	

Additionally, two simplified O2I building penetration loss models are provided in [17], a low-loss and a high-loss model, depending on the building materials. The low-loss model is given by:

$$\mathrm{PL}_{tw_{\text{low}}} = 5 - 10\log_{10}\left(0.3 \cdot 10^{\frac{-L_{\text{glass}}}{10}} + 0.7 \cdot 10^{\frac{-L_{\text{concrete}}}{10}}\right) \tag{20}$$

where L_{glass} and L_{concrete} are the material losses for glass and concrete, respectively. The material losses depend on the frequency, f_c, according with:

$$L_{\text{glass}} = 2 + 0.2 f_c \tag{21}$$

$$L_{\text{concrete}} = 5 + 4 f_c \tag{22}$$

The high loss model is given by:

$$\mathrm{PL}_{tw_{\text{high}}} = 5 - 10\log_{10}\left(0.7 \cdot 10^{\frac{-L_{\text{IRRglass}}}{10}} + 0.3 \cdot 10^{\frac{-L_{\text{concrete}}}{10}}\right) \tag{23}$$

where L_{IRRglass} is the penetration loss of infrared-reflective glass:

$$L_{\text{IRRglass}} = 23 + 0.3 f_c \tag{24}$$

In this work, an intermediate model is used, where both models (high and low-loss) contribute 50% to the total building penetration loss. The rationale is to take into account the heterogeneity of real UMa and UMi environments considered in this work.

B. mmMAGIC PATH LOSS MODEL

The mmMagic path loss model [19] resulted from a consortium of industry, research centers, and universities in a forefront project towards developing a channel model aligned with the 5G propagation requirements. It has adopted the channel modeling methodology of the 3GPP 3D model (3GPP TR36.873 [32]), and it used, as a basis, the QuasiDeterministic Radio Channel Generator

(QuaDRiGa) model [33]. The path loss model was developed using measurement campaigns between 6 GHz and 100 GHz in various propagation scenarios.

The mmMagic path loss model is valid for the UMi and indoor scenarios. Again, for each propagation scenario, the path loss expressions are different depending on whether the UE has LoS, or not, to the BS. Also, the UMi path loss model follows the ABG modeling with a log-normal SF distribution, as presented in Table 3.

The O2I building penetration loss is modeled from the 3GPP low and high-loss models with one additional term to account for the elevation angle (θ) loss: $L_{el} = 20\,|\theta/90°|$ [19].

Table 3 presents the equations for both path loss models, where d_{3D} is the 3D distance between the BS and the UE, PL_1 is the path loss for distances below the breakpoint distance, d'_{BP}, PL_2 is the path loss for distances above the breakpoint distance and σ_{SF} is the SF standard deviation.

V. 5G COVERAGE ANALYSIS METRICS AND COVERAGE SCENARIOS

This section describes the metrics used for the 5G coverage analysis and the scenarios considered in rest of the work.

A. 5G COVERAGE ANALYSIS METRICS

The Reference Signal Received Power (RSRP), in dBm, is given by (based on [34]):

$$\mathrm{RSRP} = P_{\mathrm{RS}} + G_{\mathrm{BS}} - A_{\mathrm{Tx}} + G_{\mathrm{UE}} - \mathrm{PL} \tag{25}$$

where P_{RS} is the reference signal transmitted power in dBm, G_{BS} is the antenna gain in dBi (using the new beamforming model), A_{Tx} is the BS cable losses (2 dB), G_{UE} is the UE antenna gain (2.15 dBi), and PL is the path loss, in dB, from the respective path loss models.

The 5G RSRP is defined as the linear average over the power contributions of the Resource Elements (REs) carrying reference signal information [35]. In accordance, the 5G coverage analysis considers the transmitted power in the bandwidth of a single RE as a reference. The P_{RS} is given by:

$$P_{\mathrm{RS}} = P_{\mathrm{Tx,Max}} - 10\log_{10}\left(N_{\mathrm{PRB}}^{\mathrm{BW},\mu} \times 12\right) \tag{26}$$

where $P_{\mathrm{Tx,Max}}$ is the BS maximum transmitted power, in dBm, $N_{\mathrm{PRB}}^{\mathrm{BW},\mu}$ is the number of Physical Resource Blocks (PRBs) for bandwidth BW, and numerology μ [36], and 12 is the number of sub-carriers in one PRB.

The percentage of covered area is obtained by comparing the RSRP with the receiver sensitivity, $P_{\mathrm{Rx,Sens}}$, after adding the Shadow Fading (SF) margin, M_F (in dB), and the rain attenuation margin M_R (in dB), to the latter. The receiver sensitivity was calculated according to [37]:

$$P_{\mathrm{Rx,Sens}} = -174 + 10\log_{10}(\mathrm{SCS}) + N_F + \mathrm{SNR} \tag{27}$$

where -174 is the thermal noise constant in dBm/Hz, SCS is the Subcarrier Spacing (SCS) (according to μ), N_F is the receiver noise figure (9 dB), and SNR is the Signal-to-Noise Ratio (SNR), in dB, calculated using Shannon's formula [38], with a target throughput of 100 Mbps. Thus, for frequencies in the 3.5 GHz band, for a maximum bandwidth of 100 MHz, the respective SNR was 0 dB, while for the 28 GHz band (maximum bandwidth of 400 MHz), the obtained SNR was -7.23 dB.

The SF margin, M_F, guarantees a 95% cell area coverage probability and is calculated assuming a Gaussian distribution with a standard deviation of σ_{SF}, which depends on the path loss model (see Table 3). The rain margin, M_R, was calculated for a link availability of 99.95% of the time [39].

The throughput, *Thput*, was calculated to evaluate the Quality of Service (QoS) for UEs, according to [40]:

$$\begin{aligned} Thput &= 10^{-6} \cdot \sum_{i=1}^{K} \\ &\times \left(v_{\mathrm{layers}}^{(i)} \cdot Q_m^{(i)} \cdot f^{(i)} \cdot R_{\max} \cdot \frac{N_{\mathrm{PRB}}^{\mathrm{BW},\mu} \cdot 12}{T_S^{\mu}} \cdot \left(1 - OH^{(i)}\right)\right) \end{aligned} \tag{28}$$

where K is the number of aggregated Component Carriers (CC), $R_{\max}$ is the maximum coding rate and, for each i-th CC: $v_{\mathrm{layers}}^{(i)}$ is the number of Multiple-Input Multiple-Output (MIMO) layers, $Q_m^{(i)}$ is the maximum modulation order, $f^{(i)}$ is the scaling factor, T_S^{μ} is the Orthogonal Frequency Division Multiplexing (OFDM) symbol duration in a subframe with numerology μ, and $OH^{(i)}$ is the transmission overhead. The parameters $R_{\max}$, and $Q_m^{(i)}$, are given by a lookup table of Channel Quality Indicator (CQI) versus SNR [41], considering that the SNR is calculated from the received power.

For the throughput estimation, and for the carrier frequency of 3.5 GHz, a bandwidth of 100 MHz with a SCS of 60 kHz, corresponding to 135 PRBs per subframe, was considered; for the 28 GHz carrier frequency, a bandwidth of 400 MHz with a SCS of 120 kHz, corresponding to 264 PRBs per subframe, was selected. These bandwidths correspond to the maximum standardized in 5G for the respective carrier frequencies. Furthermore, two MIMO layers were assumed in the throughput calculations. Overall, the 5G radio frame configurations, used in this work, are presented in Table 4.

TABLE 4. 5G radio frame configurations.

Frequency Range	μ	SCS [kHz]	Bandwidth [MHz]	PRB
f_c <3.0 GHz	1	30	20	51
3.0 GHz $\leq f_c \leq$ 7.125 GHz	2	60	100	135
f_c >7.125 GHz	3	120	400	264

B. SYNTHETIC SCENARIOS

The synthetic scenarios, despite being simpler approximations of reality, allow reproducible results and provide the ability to test any simulation parameter. In the scope of this work, they allow to test both path loss models (3GPP and mmMAGIC), distinct beamforming radiation patterns (see Table 1), and two frequencies, 3.5 GHz and 28 GHz.

In this section two distinct synthetic scenarios are presented; an open area and a Manhanttan-like. While the former is particular to evaluate outdoor coverage, either in LoS or NLoS, the latter allows to consider both outdoor and indoor coverage.

1) OPEN AREA

The open area testing scenario consists of 19 BSs, 3-sectorized, arranged in a hexagonal grid [17]. For the UMa scenario, the BSs antennas have a height of 25 m and an Inter-Site Distance (ISD) of 500 m, while for the UMi scenarios, the BSs height is 10 m and the ISD is 200 m; the UEs height is fixed to 1.5 m. In the open area scenario, all UEs are considered in either LoS or NLoS conditions, according to the used path loss equation (LoS/NLoS). The scenario aims to compare the outdoor coverage between LoS/NLoS conditions, for the different path loss models (3GPP/mmMAGIC).

2) MANHATTAN-LIKE

The modified Manhattan-like scenario (see Fig. 8) considers buildings and streets to create a scenario where both LoS and NLoS conditions are simultaneous present.

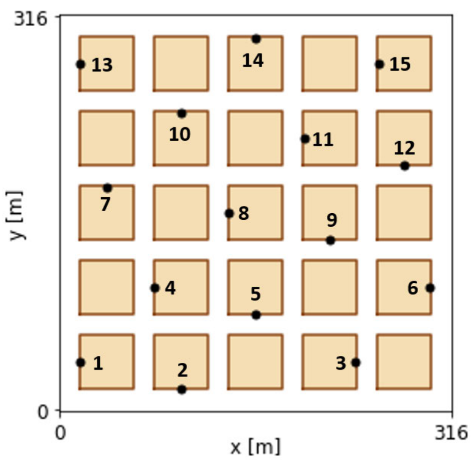

FIGURE 8. Modified Manhattan-like synthetic scenario.

The resulting Manhattan-like scenario consists of a 5 × 5 building grid, where the building width is 40 m, and the street is 20 m wide (16 m for road width and 2 m for each sidewalk width). Sidewalks (in dark brown) around the buildings (light brown) were added, separating them from the road. Buildings are 25 m in height, having eight floors; each floor is 3 m in height, and the sidewalks are 0.2 m in height. The BSs have an antenna height of 10 m and are located on lampposts in the middle of the sidewalks (*i.e.* 1 m away from the building wall and 1 m away from the road edge), which are assumed to be regularly distributed along the sidewalks.

For the sake of simplicity, in Fig. 8 only the lampposts which support the BSs are represented (black dots). The terrain is assumed to be flat.

The locations of the BSs were determined according to link budget calculations to guarantee coverage in the whole scenario. An indoor UE was considered using a carrier frequency of 28 GHz, as it is the link condition with higher path loss. In this setup, the Maximum Allowed Path Loss (MAPL) is calculated by substituting the RSRP value in (25) by the minimum power that should be received for having coverage (*i.e.*, $P_{\text{Rx,Sens}} + M_F + M_R$), and solving the equation in order to PL. With the MAPL, the NLoS UMi mmMAGIC path loss equation was used to calculate the MAPL cell radius (the building penetration loss was taken into account according to Section IV-A). Finally, with the cell radius and considering 3-sectorized sites, using the approximation of hexagonal service areas, the Inter-Site Distance (ISD) is obtained by multiplying the cell radius by 1.5 [42], resulting in 15 3-sectorized BSs with an ISD of 92.5 m. Moreover, the chosen locations for the BSs privileged LoS communications. In the Manhattan-like scenario, not only the outdoor coverage is considered but also the indoor coverage, considering UEs inside the buildings.

C. REAL SCENARIOS

For the real scenarios, both detailed 3D environment information and data from real MNOs are required, especially the location and parameters of real BSs. In this work, real sites from BSs of legacy technologies were considered, allowing to evaluate the future 5G coverage in a real scenario. The considered real scenarios were predominantly UMa scenarios, with a residual number of UMi BSs. Consequently, only the 3GPP path loss model was used as the mmMAGIC is only valid for UMi.

This section presents the real UMa environments in a Lisbon centered area using 3D geospatial data [43]. The considered geospatial data has an area of 5.5 km^2 discriminating terrain, buildings, and clutter, with a 2 m resolution, 5 m planimetric accuracy (XY), and vertical accuracy (Z) between 2 m and 3 m. The following regular and irregular urban scenarios were outlined to evaluate indoor coverage in limited areas. The third scenario is a mixed scenario where both outdoor and indoor coverage is assessed.

1) REGULAR URBAN

The regular urban area, represented in Fig. 9, is characterized by a high building density with an average height of 20.1 m, and a BS located on top of one building (blue marker), with an antenna height of 26 m.

The macro BS is used by a MNO for legacy technologies. In the regular urban scenario, only indoor coverage is assessed where the use of distinct beamforming radiation patterns are evaluated.

2) IRREGULAR URBAN

Fig. 10 presents the irregular urban scenario composed of buildings with irregular heights (average of 7.8 m), and with a nonuniform building distribution. The considered BS (blue marker) is located at 15 m height. The irregular urban

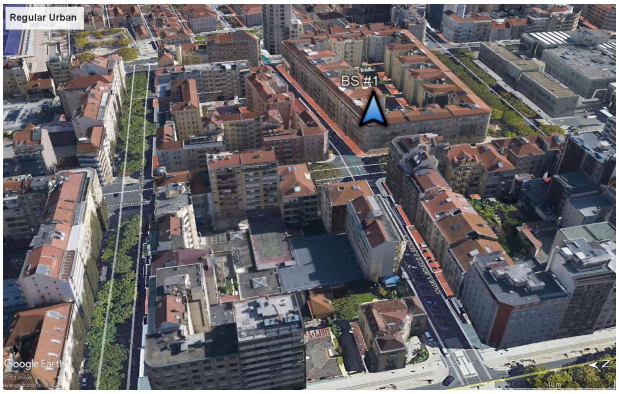

FIGURE 9. Real regular urban environment.

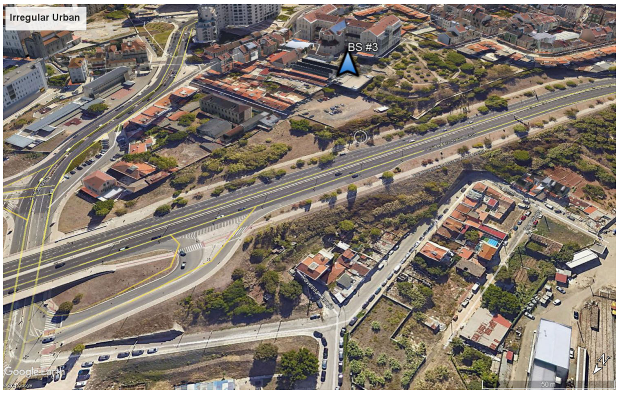

FIGURE 10. Real irregular urban environment.

scenario intends to evaluate how the environment surrounding a BS influences the optimal radiation pattern in comparison with the regular urban scenario.

3) MIXED REGULAR/IRREGULAR URBAN

The mixed regular/irregular urban scenario is presented in Fig. 11 where the considered area is limited to the locations where 3D environment data is available, represented in red. In the mixed regular/irregular urban scenario, 20 macro BSs are considered, of which 14 are 3-sectorized, while the remaining have two sectors. These BSs are real legacy sites from a Portuguese MNO. The coverage analysis is then performed considering both outdoor and indoor locations.

VI. 5G COVERAGE ANALYSIS

The 5G coverage analysis is conducted on the scenarios described in section V, evaluating the covered area, received power, and user throughput. While in the synthetic scenarios UMi deployments are considered, allowing the comparison of the 3GPP and the mmMAGIC path loss models, the real scenarios reflect UMa deployments using data from MNOs. In both cases, the impact of distinct frequencies and the effect of the different beamforming radiation patterns is assessed. Two frequency bands were considered; a mid-band frequency of 3.5 GHz, and a mmWave frequency of 28 GHz. For the 3.5 GHz frequency only the 3GPP path loss model was used, as the mmMAGIC is only valid for frequencies above 6 GHz.

FIGURE 11. Real mixed regular/irregular urban environment.

A. COVERAGE ANALYSIS USING SYNTHETIC SCENARIOS

The main goals for the coverage analysis using synthetic scenarios are the following: to compare the coverage predictions based on the 3GPP and the mmMAGIC path loss models; to compare the coverage impact of using a mid-band frequency with a mmWave frequency; to assess the beamforming coverage impact (its usage and the effect of distinct radiation patterns). The antenna configurations, presented in Table 1 (except for pattern 15), were considered. Moreover, while in the open area scenario only outdoor coverage is evaluated, separating LoS from NLoS propagation, in the Manhattan-like scenario the coverage is evaluated considering outdoor and indoor propagation. In this work, it was considered that a UE is in LoS if the 1st Fresnel Ellipsoid is at least 60% unblocked (in the full extension of the direct ray between the BS and the UE) [44].

The coverage is evaluated considering the percentage of covered area, the percentile 5% and the average of the throughput distribution, as in section V-A. The throughput statistics are calculated considering only the areas with coverage.

1) OPEN AREA

For the 3GPP and the mmMAGIC comparison, the open area scenario implements the UMi configuration described in section V-B1, with 19 BSs having an antenna height of 10 m and an ISD of 200 m.

The received power was calculated using (25), and the resulting received power Cumulative Density Function (CDF) for LoS and NLoS are depicted in Fig. 12.

Table 5 presents the percentage of covered area and the user throughput calculated as described in section V-A.

From both Fig. 12 and Table 5, the following conclusions can be stated:

- Regarding the RSRP distributions, both path loss models have similar behavior in LoS conditions; however, they differ in the NLoS case, with a 26 dB difference in the

TABLE 5. Coverage comparison, in the UMi open area, using the 3GPP and mmMagic path loss models, under distinct frequencies and antenna configurations.

Model	Frequency [GHz]	Antenna Pattern	LoS 5% Thrp. [Mbps]	LoS Avg. Thrp. [Mbps]	NLoS 5% Thrp. [Mbps]	NLoS Avg. Thrp. [Mbps]	LoS Covered Area [%]	NLoS Covered Area [%]
3GPP UMi	3.5	Kathrein	867	867	864	867	100.0	99.8
		Pattern 1	867	867	867	867	100.0	100.0
		Pattern 6	867	867	867	867	100.0	100.0
		Pattern 9	867	867	867	863	100.0	99.9
	28	Kathrein	3232	3232	67	678	100.0	2.6
		Pattern 1	3232	3232	835	1428	100.0	23.3
		Pattern 6	3232	3232	644	1874	100.0	52.5
		Pattern 9	3232	3232	67	1099	100.0	16.8
mmMAGIC UMi	28	Kathrein	3232	3232	67	100	100.0	0.5
		Pattern 1	3232	3232	67	130	100.0	1.0
		Pattern 6	3232	3232	67	422	100.0	3.3
		Pattern 9	3232	3232	67	199	100.0	1.1

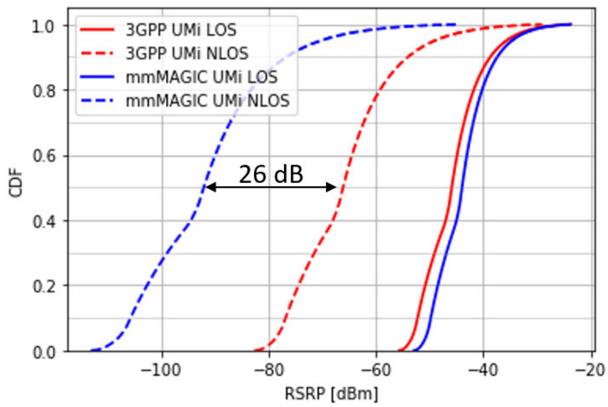

FIGURE 12. RSRP Cumulative Density Function (CDF) after applying the 3GPP UMi and mmMAGIC UMi models (28 GHz).

50% percentile for 28 GHz (see Fig. 12). In this case, the mmMAGIC NLoS model predicts higher path loss than the 3GPP. The observed power difference between the two models is in line with the results in [31].

- Concerning the covered area, in LoS conditions 100% coverage was obtained. In NLoS conditions, while at 3.5 GHz almost 100% of coverage is provided, at 28 GHz the coverage is insufficient due to the higher path loss (Table 5). So, an ISD of 200 m, in NLoS conditions, cannot provide full outdoor coverage with any of the path loss models. Moreover, at 28 GHz, a low 5% percentile of user throughput is registered when coverage is achieved, which in most simulations is below the requirement of an user data rate in the downlink of 100 Mbps [45] (measured as the 5% point of the CDF of the user throughput).
- Concerning the antenna configuration, while for LoS, 100% of the covered area was always attained, considering the NLoS (see Table 5), the use of beamforming antennas compared with a traditional single-beam antenna (Kathrein) enables a higher coverage percentage, due to higher directivity and gains. Regarding the throughput results, in NLoS conditions, beamforming led to higher throughput, particularly on pattern 6, at 28 GHz; this pattern outperforms pattern 9, which has two vertical beams instead of one, and pattern 1, which has a narrower vertical HPBW.

2) MANHATTAN-LIKE SCENARIO

The Manhattan-like scenario has 15 BSs, with antenna heights of 10 m, and with an ISD of 92.5 m (see section V-B2). The main difference in the Manhattan-like scenario, compared with the open area, is that LoS/NLoS propagation are jointly evaluated, since buildings are considered as propagation obstacles.

In the Manhattan-like scenario, the 3GPP and mmMAGIC UMi path loss models were used according to the LoS/NLoS conditions. Moreover, the respective indoor path loss models were used for the building areas. Besides the outdoor and indoor path losses, the losses due to the building walls were modeled by the 3GPP O2I penetration models (see Section IV-A). Fig. 13 represents the resulting RSRP in a vertical cut between a BS and a building.

The influence of the mentioned propagation mechanisms can be noticed, as well as the effect of the beamforming antenna, using the model from Section III-B.

Table 6 presents the throughput estimation (average and percentile 5%) for outdoor and indoor locations. Moreover, the BSs ISD was determined using a link budget dimensioned for 100% indoor coverage; thus, full coverage is attained in the whole scenario.

From Table 6, the following conclusions can be drawn:

- The throughput comparison, between considering the 3GPP or the mmMAGIC path loss models, shows fewer differences considering the NLoS scenario (see section VI-A1). Moreover, the geometry of the Manhattan-like scenario confers a larger area in LoS than in NLoS. Thus, considering that the LoS path loss predicted by the 3GPP model tends to be higher than the mmMAGIC model, it leads to higher throughput values when using the mmMAGIC model.

TABLE 6. User throughput comparison in the Manhattan-like scenario using the 3GPP and mmMagic path loss models, under distinct frequencies and antenna configurations.

Model	Frequency [GHz]	Antenna Pattern	Outdoor 5% Thrp. [Mbps]	Outdoor Avg. Thrp. [Mbps]	Indoor 5% Thrp. [Mbps]	Indoor Avg. Thrp. [Mbps]
3GPP UMi	3.5	Kathrein	224	714	18	333
		Pattern 1	224	704	18	346
		Pattern 6	282	761	18	349
		Pattern 9	224	723	18	342
	28	Kathrein	1074	2799	66	833
		Pattern 1	1192	2747	67	870
		Pattern 6	1050	2850	67	898
		Pattern 9	1450	2817	67	852
mmMagic UMi	28	Kathrein	2032	2883	66	874
		Pattern 1	2232	2983	67	1008
		Pattern 6	1974	2960	67	1046
		Pattern 9	2232	2985	67	930

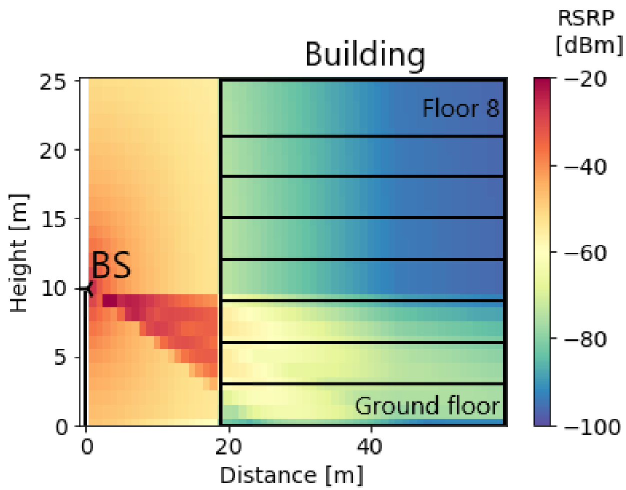

FIGURE 13. Side view of the Manhattan-like scenario with pattern 9.

- The UMi open area scenario (section V-B1) is defined by an ISD of 200 m. In the Manhattan-like scenario, after the dimensioning of the link budget for indoor coverage with a carrier frequency of 28 GHz, an ISD of 92.5 m was determined. Particularly at mmWave frequencies, the BSs density is a critical factor to provide seamless 5G radio coverage. The average outdoor and indoor peak throughput is 761 Mbps and 349 Mbps, respectively, with a carrier frequency of 3.5 GHz. At 28 GHz, the average outdoor and indoor peak throughput is 2.85 Gbps and 898 Mbps, respectively, considering the 3GPP path loss model and the antenna pattern 6. The 28 GHz frequency, despite higher path loss, benefits from the additional available bandwidth to deliver higher throughput.
- The use of beamforming led, in most cases, to higher throughput, independently of the used pattern. Pattern 6 achieves the highest throughput values. Although, in indoor scenarios, pattern 9 (with two vertical beams) could be expected to provide higher indoor coverage, its lower horizontal HPBW limits coverage in the horizontal plane. Overall, for the different configurations to achieve the best possible throughput, the number of beams and the respective horizontal and vertical HPBWs need to be aligned with the geometry of the considered scenario.
- Finally, comparing the outdoor and the indoor coverage, even the 5% percentile throughput for outdoor is above 224 Mbps, using the 3.5 GHz, and reaches at least 1 Gbps when considering 28 GHz. For the indoor coverage, average throughput values around 300 Mbps and 800 Mbps are achieved, for 3.5 GHz and 28 GHz, respectively. Nevertheless, the indoor 5% percentile throughput is below the 100 Mbps downlink requirement for the user data rate [45].

In conclusion, a significant difference is observed in NLoS conditions between the 3GPP path loss and the mmMAGIC path loss models. However, since for the synthetic scenario outdoor coverage is mostly done in LoS conditions this fact has little impact in the results depicted in Table 6. Network densification is required to deploy mmWave frequencies, so that gigabit per second throughput can be obtained, even in indoor scenarios. Coverage and user throughput are enhanced when using beamforming, which is taken into account using beamforming antenna models as presented in section III.

B. COVERAGE ANALYSIS USING REAL SCENARIOS

The 5G coverage analysis in real scenarios aims to evaluate the indoor coverage and global coverage (outdoor and indoor), using BSs locations from real MNO of legacy technologies. In the following scenarios, UMa deployments are considered, as the locations of UMi deployments are residual in the study area. Consequently, only the 3GPP path loss model is used, as the mmMAGIC is not valid for UMa scenarios.

The indoor coverage analysis examines the radio propagation using the 3.5 GHz frequency, the impact of the radiation patterns and antenna configuration parameters, and the antenna tilt influence. The regular and irregular scenarios (see section V-C) are considered.

For the global coverage analysis, the mixed regular/irregular urban scenario (section V-C) is used considering three distinct frequencies, 700 MHz, 3.5 GHz, and 28 GHz.

1) REGULAR URBAN

The regular urban scenario, presented in section V-C1, is characterized by a BS with an antenna height of 26 m and an average surrounding buildings height of 20.1 m. The beamforming radiation pattern 1 and 9 are considered to evaluate the impact of multiple vertical beams. Moreover, the indoor coverage is calculated according to different tilt values and distinct vertical scanning ranges of beams (delimiting the maximum and minimum vertical angle where energy is radiated by the vertical beams). A lower vertical scanning range of beams forces the radiated power to a narrower vertical area, while a higher scanning range allows the radiated power to a broader vertical area.

For the environment presented in Fig. 9, the indoor coverage area (in percentage) was calculated using the 3GPP path loss model, taking into account the losses due to outdoor propagation, building penetration, and indoor propagation. Two vertical scanning ranges with an amplitude of 15° and 30° were compared, and tilt values, varying from 0° to 12°, were also evaluated. The resulting indoor coverage percentages for the radiation pattern 1 are presented in Fig. 14.

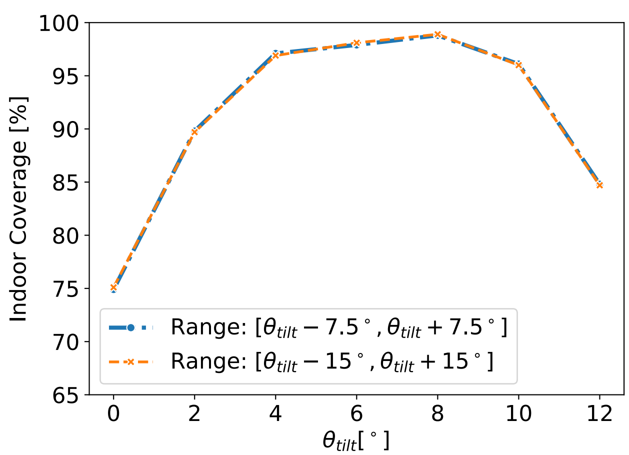

FIGURE 14. Regular urban indoor coverage as a function of the applied downtilt (pattern 1).

Since the considered beamforming pattern has just one vertical beam, changing the vertical scanning range did not affect the indoor coverage percentage, as both curves overlap. With lower downtilt values, the indoor coverage is smaller, but as the downtilt increases, the radiation pattern is best pointed in the direction of the buildings, and almost full indoor coverage is attained. When the downtilt is high, the radiation pattern points to the ground, deteriorating the indoor coverage again.

Fig. 15 details the indoor coverage results for pattern 9.

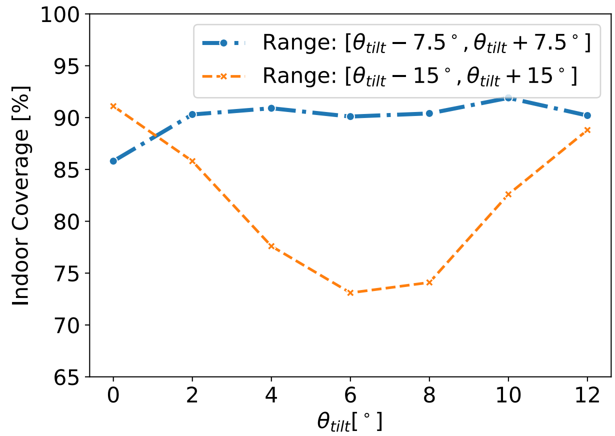

FIGURE 15. Regular urban indoor coverage as a function of the applied downtilt (pattern 9).

For pattern 9, the scanning ranges provide different results; the radiation pattern with the range $[\theta_{tilt} - 15°, \theta_{tilt} + 15°]$ and 0° tilt behaves as pattern 1 with a two degree tilt, as the lower vertical beam points to the buildings whereas the upper beam points to the sky. As the downtilt increases, the lower beam starts pointing to the bottom of the buildings, while the upper beam does not point yet in the direction where most buildings would be covered, so the indoor coverage deteriorates. When the maximum of the upper beam radiates to the top of the building, indoor coverage improves. With a smaller vertical scanning range of beams, $[\theta_{tilt} - 7.5°, \theta_{tilt} + 7.5°]$, indoor coverage is almost constant around 90%. The wider the vertical scanning range of beams, the more dispersed is the radiated energy. Thus, with the smaller range, the radiated energy is focused around the tilt angle. There are variations presented in the $[\theta_{tilt} - 7.5°, \theta_{tilt} + 7.5°]$ range, but they are much smaller. Therefore, it can be concluded that having a wider range of beams may not always be beneficial due to the higher energy dispersion.

The use of multiple vertical beams did not improve the indoor coverage, compared with a single vertical beam pattern, despite evaluating distinct tilt values and vertical scanning ranges. To further judge the coverage impact of multiple vertical beams, a new scenario is introduced in Fig. 16.

The scenario is defined by a hotel (light gray), with a height of 92 m, and a BS on a nearby building (80 m away), with an antenna height of 26 m. The indoor coverage analysis is performed as described in the previous scenario. However, it considers only the indoor of the high-rise building, with the following considerations: a tilt angle such that the radiation diagram points to the middle of the building; a new radiation pattern (pattern 15), with four vertical beams and two horizontal beams. This pattern is adapted to high-rise buildings and hotspot coverage and not to widespread coverage, as the remaining radiation patterns.

The resulting indoor coverage for the reference building, using pattern 1, was 58.7%; this percentage increases to 83.1% for pattern 9. As the area of interest has a height

FIGURE 16. Real high-rise building in urban environment.

greater than the width, pattern 9, with two vertical beams and a narrower horizontal HPBW, radiates more power directly to the building. This effect is even more pronounced with pattern 15, improving the indoor coverage up to 97.8%.

Overall, in regular urban deployments and considering UMa environments, radiation patterns with multiple vertical beams should be limited to particular scenarios, where buildings are higher than the BSs. Moreover, 5G with beamforming in the vertical plane can be a valid alternative to typical indoor Distributed Antenna System (DAS), used for example in high-rise buildings.

2) IRREGULAR URBAN

The irregular urban scenario, presented in section V-C2, is characterized by a BS with an antenna height of 15 m and an average buildings height of 7.8 m. Patterns 1 and 9 are evaluated as in the regular urban scenario.

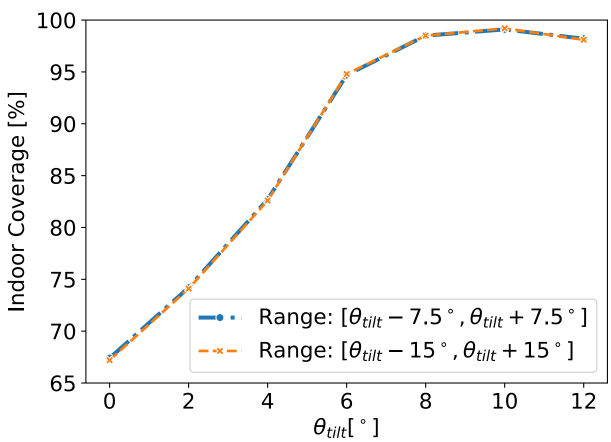

FIGURE 17. Irregular urban indoor coverage as a function of the applied downtilt (pattern 1).

Fig. 17 depicts the indoor coverage results for pattern 1. For this radiation pattern, the indoor coverage has similar behavior to the observed in the regular urban scenario. However, high downtilt values are required for almost full indoor coverage as the buildings have low heights.

Fig. 18, which depicts the indoor coverage results for pattern 9, shows that the two scanning ranges provide "symmetric" coverage. With a vertical range of $[\theta_{tilt} - 15^\circ, \theta_{tilt} + 15^\circ]$, and with small downtilt values, the indoor coverage is around 87%-90%. For higher downtilt values, the indoor coverage tends to decrease.

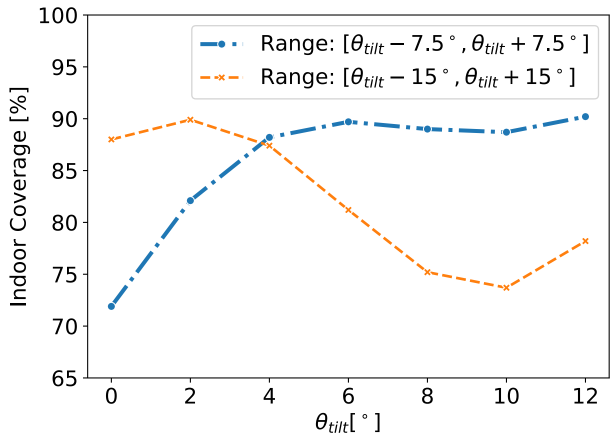

FIGURE 18. Irregular urban indoor coverage as a function of the applied downtilt (pattern 9).

With a vertical range of $[\theta_{tilt} - 7.5^\circ, \theta_{tilt} + 7.5^\circ]$, indoor coverage is lower than the previous configuration for small downtilt values, as the upper beam is pointing to the sky. When the downtilt is increased, the indoor coverage increases and remains almost constant.

Overall, in irregular UMa scenarios, pattern 1 still provides higher indoor coverage. So, radiation patterns with a single vertical beam in UMa scenarios provide the highest indoor coverage when the optimal tilt is used.

3) MIXED REGULAR/IRREGULAR URBAN

The mixed regular/irregular UMa scenario is used to assess the 5G global coverage (outdoor and indoor) in a broader area (*cf.* section V-C3), testing the 700 MHz, 3.5 GHz, and 28 GHz frequencies. The scenario comprises an area of 5.5 km^2, where real locations of 20 BSs were used.

In the previous sections, pattern 1 produced higher indoor coverage (when comparing to patterns having multiple vertical beams). So, by considering pattern 1 for the coverage analysis, the indoor coverage was maximized, and having eight horizontal beams it also enhances the outdoor coverage. The received signal was calculated for indoor and outdoor, at ground level (1.5 m), using the 3GPP path loss model for the three proposed frequencies.

In Fig. 19, the coverage prediction for the 700 MHz is presented in a 3D scenario. The percentage of the covered area was 85.7%, and the 50% percentile of the RSRP was −91.67 dBm. As expected, at a lower frequency, high coverage is achieved.

In 5G networks, the 700 MHz band will support widespread coverage and Internet of Things (IoT) services,

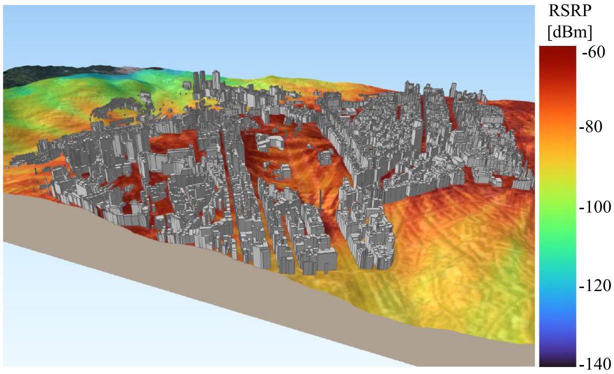

FIGURE 19. Mixed regular/irregular urban coverage prediction at 700 MHz.

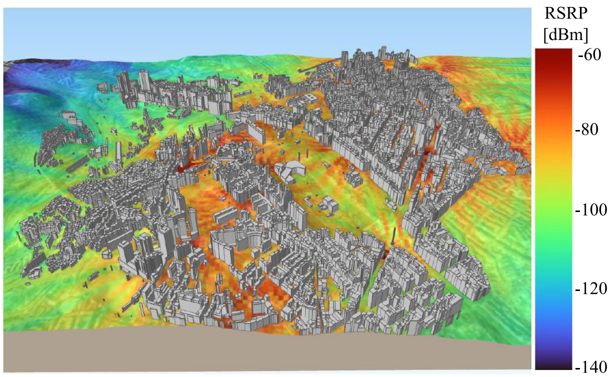

FIGURE 20. Mixed regular/irregular urban coverage prediction at 3.5 GHz.

as these have low capacity requirements. Services that require higher capacity should be provided by using higher frequency bands where more bandwidth is available.

For the carrier frequency of 3.5 GHz, the obtained results are depicted in Fig. 20.

Compared to the previous simulation, there is a decay in the RSRP due to the higher working frequency. The percentage of the covered area is reduced to 76.6%, and the 50% percentile of the RSRP was -110.0 dBm. However, the difference in the covered area is less significant when compared to the RSRP difference. At 3.5 GHz, the required SNR is lower, limiting the frequency impact on the covered area. The lower SNR, at 3.5 GHz, is due to a larger available bandwidth and thus more physical resources, easing to achieve the target throughput of 100 Mbps.

The spectrum between 3.4 GHz and 3.8 GHz is expected to emerge as the primary frequency band for the first 5G deployments and services, offering a good balance between coverage and capacity. Additionally, early network deployments co-located with existing BSs from legacy technologies, where the existing infrastructure is shared, allow a cost-efficient deployment.

The results of the final frequency, 28 GHz, are depicted in Fig. 21. Again, as the frequency increases, the RSRP

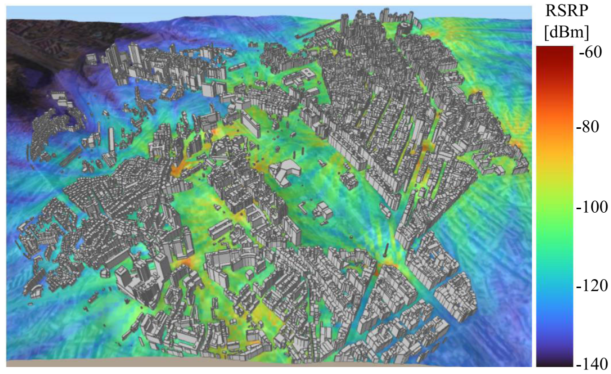

FIGURE 21. Mixed regular/irregular urban coverage estimation at 28 GHz.

TABLE 7. Mixed regular/irregular urban scenario results.

Frequency [GHz]	Covered Area [%]	Median Power [dBm]
0.7	85.7	-96.7
3.5	76.6	-110.0
28	23.8	-131.1

decays to a RSRP of -131.12 dBm (50% percentile), and the percentage of the covered area to 23.8%.

The comparison between the different frequencies is summarized in Table 7.

The mmWave frequencies will play an important role in 5G to fulfill the International Mobile Telecommunications - 2020 (IMT-2020) vision, notably to support ultra-high-speed mobile broadband. However, due to high propagation losses at mmWaves, which are visible in Fig. 21, MNOs must invest considerably in network densification, mainly in urban and dense urban areas. The densification of mmWave BSs will essentially occur at micro- and small-cell levels using urban furniture such as lampposts, bus stops, and traffic signs.

VII. 5G DRIVE TEST CALIBRATION

Often, the path loss predictions from stochastic propagation models and the path loss obtained by signal measurements show significant differences. The stochastic path loss models are based on extensive measurement campaigns. However, these campaigns are dependent on the specific geographical area (*e.g.,* heavy clutter or other topological peculiarities), frequency band, and weather conditions. For better network coverage prediction, the path loss parameters should be calibrated for each geographical location.

In this section, the UMa 3GPP path loss model is calibrated using real DTs measurements from 3.7 GHz and 26 GHz frequencies. The calibration of the mmMAGIC required UMi measurements that were unavailable, constituting future work. Moreover, the scenario V-B1 is analyzed using the UMa specification and the 3GPP calibrated path loss model. Finally, regression ML algorithms are used to increase prediction accuracy with data-driven path loss models.

A. DRIVE TEST CAMPAIGNS

The 3GPP path loss model was calibrated with three distinct DT campaigns: one using a carrier frequency of 3704.82 MHz and two with a carrier frequency of 26500.08 MHz, all in UMa environments. The first DT campaign (at 3.7 GHz) resulted from three sites (a total of four sectors) with BSs antenna heights of 20 m. The second and third DT campaigns concern one sector each, with a BS antenna height of 30 m and 15 m, respectively. Even though the available DT measurements do not correspond exactly to the same frequencies used in Section VI, the difference is small enough to retain the main conclusions.

The DT campaigns were performed in dedicated mode, using a smartphone with a Qualcomm chipset and XCAL [46] as a DT tool to automatically record and decipher messages from the air interface, including the 5G RSRP of the respective serving cells.

Firstly, information regarding terrain and buildings (geospatial data) was obtained from public data sources and used to assess whether each DT measurement (data point) was in LoS or NLoS to the respective BS. The DT measurements, recording the 5G RSRP, corresponding to the first DT campaign, are presented in Fig. 22, while the second and third DT campaigns are depicted in Fig. 23 and Fig. 24, respectively.

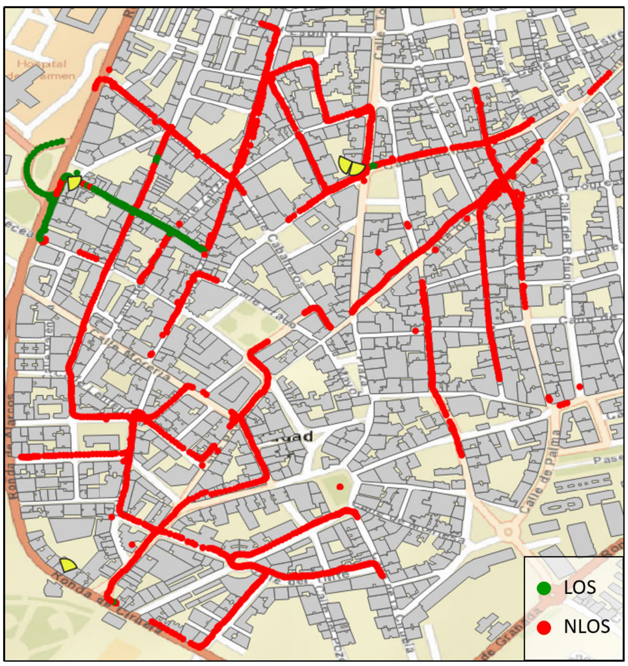

FIGURE 22. DT campaign with LoS/NLoS classification at 3.7 GHz (four sectors with an antenna height of 20 m).

Since the real DTs measure the $\mathrm{RSRP}_{\mathrm{meas}}(t)$, at time t, the correspondent path loss, $\mathrm{MPL}(t)$, was computed, in dB, as:

$$\mathrm{MPL}(t) = P_{\mathrm{RS}} + G_{\mathrm{BS}} + G_{\mathrm{UE}} - \mathrm{RSRP}_{\mathrm{meas}}(t) \quad (29)$$

where P_{RS} is the reference signal transmitted power in dBm, G_{BS} is the BS antenna gain in dBi, and G_{UE} is the UE antenna

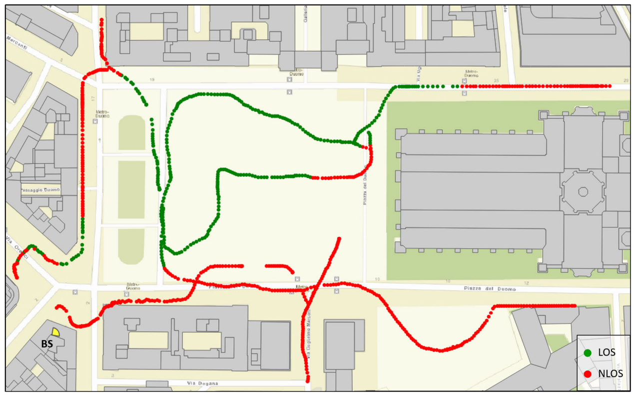

FIGURE 23. DT campaign with LoS/NLoS classification at 26 GHz (one sector with an antenna height of 30 m).

FIGURE 24. DT campaign with LoS/NLoS classification at 26 GHz (one sector with an antenna height of 15 m).

gain in dBi. The antenna gain of the BS (G_{BS}) was computed using the beamforming model proposed in section III, for the considered antenna pattern (pattern 6) using (6), (7) and (11), and with (ϕ, θ) corresponding to the direction between the BS and the point where the measurement was obtained. Pattern 6 has a broad horizontal coverage as it contains eight horizontal beams and one vertical beam, with a maximum antenna gain of 25 dBi.

Path loss models describe the experienced average path loss while the DTs field measurements are instantaneous, including slow fading (shadowing) and fast fading (multipath). Thus, the measured path loss as a function of time, t can be modeled as:

$$\mathrm{MPL}(t) = \mathrm{PL}(t) + \mathrm{F}(t) \quad (30)$$

where $\mathrm{PL}(t)$ is the average path loss and $\mathrm{F}(t)$ denotes the fading term. Therefore, before making any comparisons between the DT measurements and the path loss model predictions, a sliding-window method was employed to filter the slow fading out [47]. The filtering process averages the measurements over a spatial and temporal range of measurements, where the mean signal (path loss) is considered constant.

Let $\mathrm{MPL}_i(t)$ be the i^{th} measured path loss. Hence, the i^{th} mean path loss $\mathrm{PL}_i(t)$ is given by:

$$\mathrm{PL}_i(t) = \frac{1}{|X|} \sum_{k=\min(X)}^{\max(X)} \mathrm{MPL}_k \tag{31}$$

where X is a measurement set:

$$X = \{n : D(\mathrm{MPL}_i(t), \mathrm{MPL}_n(t)) \leq L \wedge T(\mathrm{MPL}_i(t), \mathrm{MPL}_n(t)) \leq \Delta t\} \tag{32}$$

where function $D(\mathrm{MPL}_i(t), \mathrm{MPL}_n(t))$ calculates the distance and $T(\mathrm{MPL}_i(t), \mathrm{MPL}_n(t))$ the time difference between samples $\mathrm{MPL}_i(t)$ and $\mathrm{MPL}_n(t)$, respectively, L is the window size and Δt the time interval, corresponding to the maximum distance and time interval, respectively, where the signal is considered to be constant. The time interval is calculated based on L and v, which is the average DT speed: $\Delta t = L/v$. According to [48], L must be between 20λ and 40λ, and a value of 30λ is considered in this work.

In Fig. 25, the obtained data, after filtering, is presented. For the 3.7 GHz frequency, 2892 DT measurements were obtained, from which 239 correspond to LoS conditions. For 26 GHz, a total of 3414 measurements were collected with 1212 corresponding to LoS.

B. 3GPP MODEL CALIBRATION

In this section, the 3GPP UMa model was calibrated using DTs measurements at 3.7 GHz and 26 GHz. Two calibrations were performed: including all DT measurements (3.7 GHz and 26 GHz) in a full-spectrum model and only considering 26 GHz measurements. By having both calibrations, it is possible to evaluated how adding multiple frequencies into a single calibrated model can limit its accuracy.

All DT measurements had a distance below the breakpoint distance (1369 m for 3.7 GHz and 7020 m for 26 GHz), thus the 3GPP LoS PL_2 was not considered. Since the 3GPP UMa model (LoS PL_1 and NLoS) is an ABG type of model, linear regression was chosen to calibrate it, given by:

$$\mathrm{PL} = 10\alpha \log_{10}(d_{3D}) + \beta + 10\gamma \log_{10}(f_c) \tag{33}$$

where α, β and γ are the model calibration parameters.

Linear regression attempts to model the linear relationship between one or more independent variables (input features) and a dependent variable (output feature). In this particular case, the input features are the 3D distance, d_{3D}, and the frequency, f_c, and the output feature is the path loss, PL. The Sum of Squared Error (SSE), between the propagation model predictions and the measured path loss, was used as the cost function to calibrate the path loss model.

The linear regression process was applied to both calibrations (multi and mono frequency) using (33). The calibration accuracy was evaluated using the MAE, the RMSE and the coefficient of determination, R^2. The obtained results are depicted in Table 8, where the LoS and NLoS measurements were calibrated separately.

The non calibrated 3GPP UMa model has a MAE, between the measured path loss and the predicted, of 21.05 dB and 14.48 dB for LoS and NLoS, respectively. Comparing with the calibrated full-spectrum model, the prediction MAE is reduced to 5.45 dB and 7.51 dB, for LoS and NLoS, respectively, while the 26 GHz calibrated model obtained MAEs, respectively, of 5.00 dB and 7.16 dB. The error analysis taking as reference the RMSE is similar, and the coefficient of determination attains values above 0.50 in the calibrated models. Considering the calibrated model parameters, it can be noted that the distance coefficient, α, has a value of 4.53 in LoS conditions. In LoS, it should be close to the free space propagation coefficient of 2, however, in the calibrated model, the excessive value of α is balanced with lower values of β, which is only an optimization parameter. Additionally, it has to be considered that the model calibration process, using Ordinary Least Squares (OLS), is solely dependent on the available drive test data (quantity and quality). From the quantity point of view, the DT measurements contain fewer LoS measurements than NLoS, which influence the calibrated parameters of the LoS models (the NLoS calibrated model parameters exhibit fewer deviations than the LoS models). Moreover, the path loss was obtained considering (29), where the antenna model to estimate G_{BS} can introduce error on the retrieved path loss. However, the accuracy of the original path loss model is low, and it is worthy to calibrate the model even when the above considerations are verified.

The calibration increases the prediction accuracy significantly, and even calibrating with multiple frequencies the obtained accuracy is similar to a single frequency calibrated model. The multiple frequency calibration has the advantage of having the frequency dependent parameter calibrated, enabling the model to be used with other frequencies.

C. APPLYING THE 3GPP CALIBRATED MODEL

In the previous section, it was concluded that the calibrated path loss model, allow for improving the prediction accuracy. Consequently, the use of such model improves the realism of path loss dependent analysis. So, the analysis of the UMa open area synthetic scenario from section V-B1 was performed using the 3GPP full-spectrum calibrated model. Regarding the used antenna configurations, besides the legacy antenna (Kathrein), only pattern 6 for the beamforming antenna was used, as it has only one vertical beam, suited for a UMa scenario. The respective coverage analysis result is presented in Table 9.

The result analysis reveals that the estimated throughput with the non calibrated model is significantly higher compared to the calibrated model. The frequency comparison reveals a higher difference in the 26 GHz band. From the average throughput analysis, differences between 2% and 163% (using the calibrated model as reference) are registered, depending on the antenna and the frequency. For the percentages of covered areas, a general increase is noticed when using the non calibrated model, going up to 25%, discarding the cases of low covered areas.

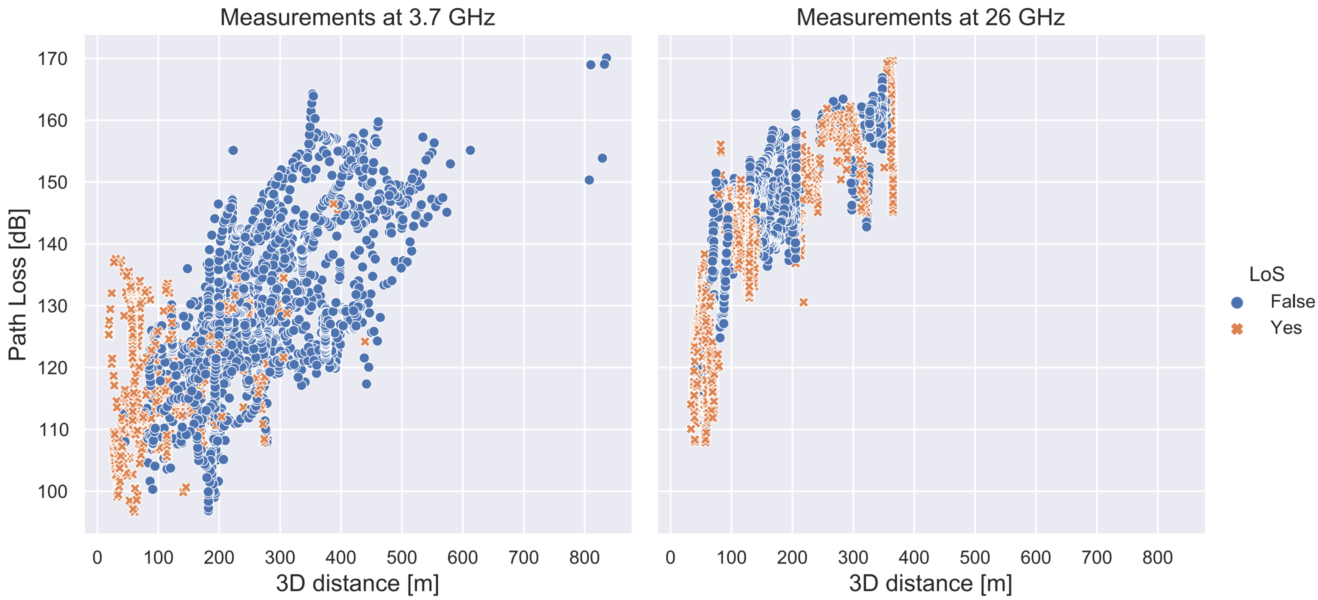

FIGURE 25. DT measurements with path loss as a function of the distance for frequencies 3.7 GHz and 26 GHz.

TABLE 8. Calibration of the 3GPP path loss model.

	3GPP UMa		Calibrated Full-Spectrum Model		Calibrated 26 GHz Model	
Parameter	LoS	NLoS	LoS	NLoS	LoS	NLoS
α	2.20	3.91	4.53	3.8	4.71	3.78
β[dB]	28.00	13.54	20.87	24.67	-5.45	31.78
γ	2.00	2.00	0.40	2.46	2.00	2.00
MAE[dB]	21.05	14.48	5.45	7.51	5.00	7.16
RMSE[dB]	23.42	16.66	7.26	9.17	7.08	8.71
R^2	-	-	0.50	0.58	0.56	0.53

TABLE 9. User throughput and percentage of covered area in UMa open area scenario with calibrated models.

Frequency [GHz]	Antenna Pattern	Calibrated Model	LoS 5% Thrp. [Mbps]	LoS Avg. Thrp. [Mbps]	NLoS 5% Thrp. [Mbps]	NLoS Avg. Thrp. [Mbps]	LoS Covered Area [%]	NLoS Covered Area [%]
3.7	Kathrein	Yes	389	684	320	556	93.33	80.34
		No	864 (122%)	866 (27%)	727 (127%)	842(52%)	100 (8%)	100 (25%)
	Pattern 6	Yes	729	847	650	824	99.44	99.04
		No	868 (19%)	864 (2%)	867 (33%)	867 (5%)	100 (1%)	100 (1%)
26	Kathrein	Yes	382	1287	67	84	17.32	0.48
		No	2729 (614%)	3139 (144%)	67 (0%)	221 (163%)	100 (488%)	0.49 (1%)
	Pattern 6	Yes	1192	2538	67	399	86.41	0.78
		No	3222 (170%)	3213 (27%)	67 (0%)	1050 (163%)	100 (16%)	1.08 (39%)

Overall, the non calibrated 3GPP model leads to overestimating both coverage and user QoS metrics.

D. MACHINE LEARNING BASED MODELS

In this section, ML regression algorithms were used to develop data-based path loss models, using the DT measurements presented in section VII-A. Also, a comparison with the calibrated 3GPP model is presented. Two models considering full-spectrum measurements (3.7 GHz and 26 GHz measurements) for LoS and NLoS, respectively, and two models for 26 GHz measurements (LoS and NLoS) were developed. The full-spectrum models estimate the path loss based on the 3D distance, d_{3D}, and frequency, f_c, while the 26 GHz models consider only the 3D distance as input.

When using ML, it is common to divide the data into a training set and a testing set. The training set, $(x_1, y_1), \ldots, (x_m, y_m) \subset \mathbb{X} \times \mathbb{R}$, where $\mathbb{X}$ denotes the space of the input patterns (*e.g.*, $\mathbb{X} = \mathbb{R}^d$) and y the respective feature output. The training set data is used to train the model, and the test set data to access its accuracy. In this case, the whole data was divided randomly between training (80%) and testing (20%). Two ML algorithms were considered; the Support Vector Regression (SVR) [49] and the RF [50].

The SVR is a non-linear regression algorithm that introduces nonlinear traits by preprocessing the training examples x_i by using a map, $\Omega : \mathbb{X} \rightarrow \mathbb{F}$, into some feature space $\mathbb{F}$. Formally, it is given by [51]:

$$f(x) = \sum_{i=1}^{m} (\alpha_i - \alpha_i^*) k(x, x_i) + b \tag{34}$$

where m is the number of training examples, α_i and α_i^* are the Lagrange Multipliers, $k(.)$ is a Kernel function ($k(x, x') := \langle \Omega(x), \Omega(x') \rangle$) and x_i is the i$^{\text{th}}$ training example. The Radial Basis Function (RBF) was used as Kernel function [52]:

$$K(x, x_i) = e^{-\gamma \|x - x_i\|^2} \tag{35}$$

where $\gamma \in \mathbb{R}$ is an SVR hyperparameter. A detailed explanation of the SVR formulation is presented in [51].

The SVR implementation from [53] was used where two additional model hyperparameters, $C \in \mathbb{R}$ and ϵ, were considered. While C is a regularization parameter, ϵ specifies the distance from the actual value where no penalty is given by the training loss function. The SVR hyperparameters were optimized by performing k-fold cross-validation [53] (with $k = 10$) in the training data.

The RF model consists on a collection of randomized base regression trees formally given by [54]:

$$f(x) = \mathbb{E}_{\Theta} [r(x, \Theta)] \tag{36}$$

where $\Theta \in \mathbb{R}^T$ is a randomizing variable, $r(,)$ is the base regression tree, and $\mathbb{E}_{\Theta}$ aggregates the regression estimate concerning the random parameter Θ_t. The variable Θ_t determines the construction of an individual regression tree, r_t, by controlling how the tree grows and splits. Also, T indicates the number of individual regression trees used for the RF estimate. The training of the RF models considers the following hyperparameters, according to the implementation provided by [53]:

- T - the number of trees in the forest;
- $Depth_{max}$ - the maximum depth of a tree;
- $Leaf_{min}$ - the minimum number of samples required to be at a leaf node;
- $Splitf_{min}$ - the minimum number of samples required to split an internal node.

The RF hyperparameters were optimized considering 10-folds for the k-fold cross-validation.

Then, both algorithms were trained using the training set, and the metrics, MAE, RMSE, and R^2, were calculated on the test set data, between the respective model prediction and the measured path loss. Also, the comparison with the path loss 3GPP model and its calibrated model is based on the test set.

The hyperparameter tuning results, after the 10-fold cross-validation, for each ML regression algorithm and each path loss data model (*i.e,* full spectrum *vs* 26 GHz and LoS *vs* NLoS) are presented in Table 10.

The overall results are presented in Table 11. The calibrated 3GPP model has the highest error in all comparisons (LoS/NLoS, multi/single frequency). Both the SVR and the RF algorithms always achieve lower prediction errors, and the RF algorithm constantly outperform the SVR.

TABLE 10. Hyperparameters for the ML regression algorithms.

ML Regression Algorithm	Hyper-parameter	26 GHz Model		Full Spectrum Model	
		LoS	NLoS	LoS	NLoS
SVR	C	1	1	1	1
	ϵ	5e-3	1e-2	5e-3	1e-1
	γ	3	20	1	10
RF	T	200	200	300	200
	$Depth_{max}$	8	25	10	25
	$Leaf_{min}$	15	15	10	15
	$Splitf_{min}$	30	30	20	30

TABLE 11. ML models' results on the respective test sets.

		Full-Spectrum Model			26 GHz Model		
		MAE	RMSE	R^2	MAE	RMSE	R^2
LoS	3GPP CAL.	9.65	12.26	0.27	8.54	9.89	0.29
	SVR	5.05	6.97	0.59	5.38	7.38	0.60
	RF	4.58	6.25	0.67	4.85	6.40	0.70
NLoS	3GPP CAL.	7.22	8.88	0.63	6.02	7.26	0.65
	SVR	5.96	8.13	0.69	4.13	5.75	0.78
	RF	5.32	7.33	0.75	3.70	4.98	0.83

When comparing the path loss models between LoS and NLoS, in NLoS, there is a general tendency to obtain lower errors, possibly due to the higher amount of measurements. When comparing the full spectrum model and the 26 GHz model, as seen in the previous section, the tendency is to have higher accuracy in the single frequency model. Overall, the lowest errors are obtained for the NLoS 26 GHz model, with a MAE of 3.70 dB, a RMSE of 4.98 dB, and a R^2 of 0.83 by the RF algorithm.

To complement the analysis, the corresponding path loss predictions of the NLoS 26 GHz model are represented against the real measurements in Fig. 26. As pointed out, the 3GPP model presents the highest error, generally predicting below the measured path loss. The calibrated 3GPP is well fitted with the measured path loss distribution. However, the most revealing analysis corresponds to the non-linear regression algorithms (SVR and RF). The respective lower errors are obtained due to the introduced non-linear dependence on the distance. The distance is known to have a linear dependence with the path loss, so the measured path loss incorporates other radio propagation effects. The environment itself is non-homogeneous with distinct building densities and heights, varying street widths, and other factors, impacting the measured path loss. Thus, from a statistical point of view, the ML algorithms incorporate part of the propagation environment characteristics. The consequence is that the ML-based models provide accurate predictions as long as the non-linear data dependence on the distance is maintained. It requires the same environment to be maintained or to be similar. The calibrated 3GPP model, which forces a linear dependence between distance and path loss, supported on a physical foundation, can be applied in more scenarios, as long as the main characteristics of the original propagation environment are kept.

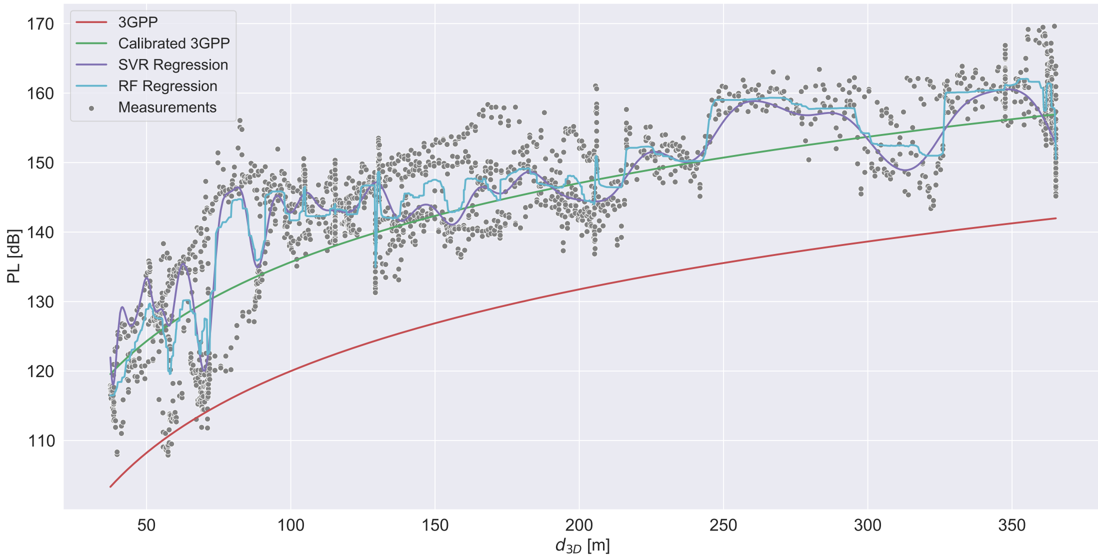

FIGURE 26. Path loss model comparison for NLoS 26 GHz measurements.

VIII. CONCLUSION

Path loss and antenna models play an essential role in mobile network planning and coverage prediction, particularly in early network deployment stages, as the current 5G. New path loss models have been proposed, as the 3GPP TR 38.901 and the mmMAGIC. The comparison between both evidenced that these models' path loss predictions are similar except in NLoS conditions where the mmMAGIC predicts higher path loss. Furthermore, the 5G coverage was assessed in a new UMi Manhattan-like scenario, with an ISD around 100 m, which provides coverage even in an indoor environment at 28 GHz. However, average gigabit/s throughput is not achieved with lower frequencies, as the 3.5 GHz.

The 5G enhances coverage by using beamforming antennas. A new antenna model has been used to model beamforming and was evaluated in several scenarios. The use of multiple vertical beams has been found beneficial in scenarios where the BS height is lower than the average building heights, or in specific hotspot areas, as in high-rise buildings. For typical UMa deployments, antenna configurations with one vertical beam are preferable as they provide good indoor coverage and maximize the outdoor covered area. Nevertheless, the antenna tilt is paramount to beamforming antennas, as distinct antenna radiation patterns require particular tilt configurations, according to the surrounding environment geometry.

The use of 5G DT measurement campaigns allowed an evaluation of the UMa 3GPP TR 38.901 path loss model accuracy. With DT measurements at 3.7 GHz and 26 GHz, the MAE between the real measurements and the model predictions was 21.05 dB and 14.48 dB for LoS and NLoS conditions. The model calibration reduced the MAE to 5.45 dB and 7.51 dB for LoS and NLoS, respectively. Moreover, the comparison between the non-calibrated and calibrated 3GPP model revealed that the uncalibrated model leads to overestimating covered area up to 25%, and user throughput up to 163% (in the considered UMa scenario). The use of ML algorithms, to develop data-based path loss models, increased path loss prediction accuracy. In this case, and considering a subset of the total measurements, the RF algorithm surpasses both the 3GPP calibrated model and the SVR with the highest accuracy, measured by a MAE of 3.70 dB in NLoS conditions at a carrier frequency of 26 GHz.

Future work will concentrate on ML-based path loss models, as concerns of lack of generalization to other BSs or other environments still need to be addressed. Additionally, new DT measurements will allow the evaluation of the mmMAGIC path loss model for UMi and small-cell deployments.

ACKNOWLEDGMENT

The authors would like to thank to Instituto de Telecomunicações (IT) and to Celfinet for the support and contributions to this work.

REFERENCES

[1] M. Rebato, J. Park, P. Popovski, E. D. Carvalho, and M. Zorzi, "Stochastic geometric coverage analysis in mmWave cellular networks with realistic channel and antenna radiation models," *IEEE Trans. Commun.*, vol. 67, no. 5, pp. 3736–3752, May 2019.

[2] J. M. Kelner and C. Zióákowski, "Path loss model modification for various gains and directions of antennas," in *Proc. 12th Eur. Conf. Antennas Propag. (EuCAP)*, 2018, pp. 1–4.

[3] M. Rebato, L. Resteghini, C. Mazzucco, and M. Zorzi, "Study of realistic antenna patterns in 5G mmWave cellular scenarios," in *Proc. IEEE Int. Conf. Commun. (ICC)*, May 2018, pp. 1–6.

[4] X. Yu, J. Zhang, M. Haenggi, and K. B. Letaief, "Coverage analysis for millimeter wave networks: The impact of directional antenna arrays," *IEEE J. Sel. Areas Commun.*, vol. 35, no. 7, pp. 1498–1512, Jul. 2017.

[5] J. Kim, J. Park, S. Kim, S.-L. Kim, K. W. Sung, and K. S. Kim, "Millimeter-wave interference avoidance via building-aware associations," *IEEE Access*, vol. 6, pp. 10618–10634, Feb. 2018.

[6] J. Huang, Y. Liu, C.-X. Wang, J. Sun, and H. Xiao, "5G millimeter wave channel sounders, measurements, and models: Recent developments and future challenges," *IEEE Commun. Mag.*, vol. 57, no. 1, pp. 138–145, Jan. 2019.

[7] A. Alves, M. Sousa, P. Vieira, M. P. Queluz, and A. Rodrigues, "A new 3D beamforming antenna model for 5G propagation modeling based on real data," in *Proc. 23rd Int. Symp. Wireless Pers. Multimedia Commun. (WPMC)*, Oct. 2020, pp. 1–6.

[8] C.-X. Wang, J. Bian, J. Sun, W. Zhang, and M. Zhang, "A survey of 5G channel measurements and models," *IEEE Commun. Surveys Tuts.*, vol. 20, no. 4, pp. 3142–3168, 4th Quart., 2018.

[9] S. A. Busari, K. M. S. Huq, S. Mumtaz, L. Dai, and J. Rodriguez, "Millimeter-wave massive MIMO communication for future wireless systems: A survey," *IEEE Commun. Surveys Tuts.*, vol. 20, no. 2, pp. 836–869, 2nd Quart., 2018.

[10] I. A. Hemadeh, K. Satyanarayana, M. El-Hajjar, and L. Hanzo, "Millimeter-wave communications: Physical channel models, design considerations, antenna constructions, and link-budget," *IEEE Commun. Surveys Tuts.*, vol. 20, no. 2, pp. 870–913, 2nd Quart., 2018.

[11] A. N. Uwaechia and N. M. Mahyuddin, "A comprehensive survey on millimeter wave communications for fifth-generation wireless networks: Feasibility and challenges," *IEEE Access*, vol. 8, pp. 62367–62414, 2020.

[12] I. Ahmed, H. Khammari, A. Shahid, A. Musa, K. S. Kim, E. De Poorter, and I. Moerman, "A survey on hybrid beamforming techniques in 5G: Architecture and system model perspectives," *IEEE Commun. Surveys Tuts.*, vol. 20, no. 4, pp. 3060–3097, 4th Quart., 2018.

[13] R. Schwarz, "Millimeter-wave beamforming: Antenna array design choices & characterization," Rohde & Schwarz, Munich, Germany, White Paper 1MA276_2e, Oct. 2016, version 1.0.

[14] S. Ghosh and D. Sen, "An inclusive survey on array antenna design for millimeter-wave communications," *IEEE Access*, vol. 7, pp. 83137–83161, 2019.

[15] S. Sun, T. S. Rappaport, S. Rangan, T. A. Thomas, A. Ghosh, I. Z. Kovacs, I. Rodriguez, O. Koymen, A. Partyka, and J. Jarvelainen, "Propagation path loss models for 5G urban micro- and macro-cellular scenarios," in *Proc. IEEE 83rd Veh. Technol. Conf. (VTC Spring)*, May 2016, pp. 1–6.

[16] S. Sun, T. A. Thomas, T. S. Rappaport, H. Nguyen, I. Z. Kovacs, and I. Rodriguez, "Path loss, shadow fading, and line-of-sight probability models for 5G urban macro-cellular scenarios," in *Proc. IEEE Globecom Workshops (GC Wkshps)*, Dec. 2015, pp. 1–7.

[17] *Study on Channel Model for Frequencies From 0.5 to 100 GHz (Release 16)*, 3rd Generation Partnership Project (3GPP), Technical Specification, document (TS) 38.901, Dec. 2019, version 16.1.0. [Online]. Available: https://portal.3gpp.org

[18] T. S. Rappaport, G. R. Maccartney, M. K. Samimi, and S. Sun, "Wideband millimeter-wave propagation measurements and channel models for future wireless communication system design," *IEEE Trans. Commun.*, vol. 63, no. 9, pp. 3029–3056, Sep. 2015.

[19] mmMAGIC Project, *Measurement Results and Final mmMAGIC Channel Models*, 5GPP, document ICT-671650, 2017.

[20] M. Xiao, S. Mumtaz, Y. Huang, L. Dai, Y. Li, M. Matthaiou, G. K. Karagiannidis, E. Björnson, K. Yang, I. Chih-Lin, and A. Ghosh, "Millimeter wave communications for future mobile networks," *IEEE J. Sel. Areas Commun.*, vol. 35, no. 9, pp. 1909–1935, Sep. 2017.

[21] A. Maltsev, R. Maslennikov, A. Sevastyanov, A. Khoryaev, and A. Lomayev, "Experimental investigations of 60 GHz WLAN systems in office environment," *IEEE J. Sel. Areas Commun.*, vol. 27, no. 8, pp. 1488–1499, Oct. 2009.

[22] M. Project, *D5.1: Channel Modeling and Characterization*, MiWEBA, document FP7-ICT-608637, 2014, version 1.0.

[23] A. Turkmen, M. S. Mollel, M. Ozturk, S. Yao, L. Zhang, R. Ghannam, and M. A. Imran, "Coverage analysis for indoor-outdoor coexistence for millimetre-wave communication," in *Proc. UK/ China Emerg. Technol. (UCET)*, Aug. 2019, pp. 1–4.

[24] S. Sun, T. S. Rappaport, T. A. Thomas, A. Ghosh, H. C. Nguyen, I. Z. Kovács, I. Rodriguez, O. Koymen, and A. Partyka, "Investigation of prediction accuracy, sensitivity, and parameter stability of large-scale propagation path loss models for 5G wireless communications," *IEEE Trans. Veh. Technol.*, vol. 65, no. 5, pp. 2843–2860, May 2016.

[25] S. Dahal, M. Faulkner, H. King, and S. Ahmed, "27.1 GHz millimetre wave propagation measurements for 5G urban macro areas," in *Proc. IEEE 85th Veh. Technol. Conf. (VTC Spring)*, Jun. 2017, pp. 1–5.

[26] E. Ostlin, H.-J. Zepernick, and H. Suzuki, "Macrocell path-loss prediction using artificial neural networks," *IEEE Trans. Veh. Technol.*, vol. 59, no. 6, pp. 2735–2747, Jul. 2010.

[27] S. I. Popoola, E. Adetiba, A. A. Atayero, N. Faruk, and C. T. Calafate, "Optimal model for path loss predictions using feed-forward neural networks," *Cogent Eng.*, vol. 5, no. 1, Jan. 2018, Art. no. 1444345.

[28] S. I. Popoola, A. Jefia, A. A. Atayero, O. Kingsley, N. Faruk, O. F. Oseni, and R. O. Abolade, "Determination of neural network parameters for path loss prediction in very high frequency wireless channel," *IEEE Access*, vol. 7, pp. 150462–150483, 2019.

[29] J. Thrane, D. Zibar, and H. L. Christiansen, "Model-aided deep learning method for path loss prediction in mobile communication systems at 2.6 GHz," *IEEE Access*, vol. 8, pp. 7925–7936, 2020.

[30] P. Vieira, P. Queluz, and A. Rodrigues, "MIMO antenna array impact on channel capacity for a realistic macro-cellular urban environment," in *Proc. IEEE 68th Veh. Technol. Conf.*, vol. 1, Sep. 2008, pp. 1–5.

[31] T. Rappaport, Y. Xing, G. R. MacCartney, A. F. Molisch, E. Mellios, and J. Zhang, "Overview of millimeter wave communications for fifth-generation (5G) wireless networks-with a focus on propagation models," *IEEE Trans. Antennas Propag.*, vol. 65, no. 12, pp. 6213–6230, Dec. 2017.

[32] *Study on 3D channel model for LTE (Release 12)*, 3rd Generation Partnership Project (3GPP), Technical Specification document (TS) 36.873, Sep. 2014, version 12.0.0. [Online]. Available: https://portal.3gpp.org

[33] S. Jaeckel, L. Raschkowski, K. Börner, and L. Thiele, "QuaDRiGa: A 3-D multi-cell channel model with time evolution for enabling virtual field trials," *IEEE Trans. Antennas Propag.*, vol. 62, no. 6, pp. 3242–3256, Jun. 2014.

[34] R. T. S. Heath, R. W. Daniels, R. Clark, and M. J. Nelson, *Millimeter wave wireless communications*. Upper Saddle River, NJ, USA: Prentice-Hall, 2015.

[35] *NR; Physical Layer Measurements (Release 16)*, 3rd Generation Partnership Project (3GPP), Technical Specification, document (TS) 38.215, Dec. 2020, version 16.4.0. [Online]. Available: https://portal.3gpp.org

[36] *NR; Physical Channels and Modulation (Release 16)*, 3rd Generation Partnership Project (3GPP), Technical Specification, document (TS) 38.211, Dec. 2019, version 16.0.0. [Online]. Available: https://portal.3gpp.org

[37] *NR; General aspects for Base Station (BS) Radio Frequency (RF) for NR (Release 15)*, 3rd Generation Partnership Project (3GPP), Technical Specification, document (TS) 38.817-02, 00 2020, version 15.9.0. [Online]. Available: https://portal.3gpp.org

[38] C. E. Shannon, *A Mathematical Theory of Communication*. Champaign, IL, USA: Univ. Illinois Press, 1949.

[39] *Propagation Data and Prediction Methods Required for the Design of Terrestrial Line-of-Sight Systems*, document ITU-R Recommendation P.530-17, 2017. [Online]. Available: https://www.itu.int/dms_pubrec/itu-r/rec/p/R-REC-P.530-17-201712-I!!P DF-E.pdf

[40] *NR; User Equipment (UE) Radio Access Capabilities (Release 16)*, 3rd Generation Partnership Project (3GPP), Technical Specification, document (TS) 38.306, Mar. 2020, version 16.0.0. [Online]. Available: https://portal.3gpp.org

[41] *nrChannelEstimate*. Accessed: Jan. 28, 2021. [Online]. Available: https://www.mathworks.com/help/5g/ug/5g-nr-cqi-reporting.html

[42] R. Joyce, D. Morris, S. Brown, D. Vyas, and L. Zhang, "Higher order horizontal sectorization gains for 6, 9, 12 and 15 sectored cell sites in a $3GPP/HSPA+$ network," *IEEE Trans. Veh. Technol.*, vol. 65, no. 5, pp. 3440–3449, May 2016.

[43] Visicom. (2019). *Geospatial Data*. [Online]. Available: https://visicomdata.com/samples

[44] C. Salema, *Microwave Radio Links: From Theory to Design*. Hoboken, NJ, USA: Wiley, 2003.

[45] *Minimum Requirements Related to Technical Performance for IMT-2020 Radio Interface(s)*, International Telecommunication Union, document ITU-R M.2410-0, Nov. 2017.

[46] XCAL—World's Leading Drive Test Tool. (2021). *ACCUVER*. [Online]. Available: http://www.accuver.com/sub/products/view.php?idx=6

[47] M. D. Yacoub, *Foundations of Mobile Radio Engineering*, 1st ed. Boca Raton, FL, USA: CRC Press, 1993, ch. 4.10.

[48] W. C. Y. Lee, "Estimate of local average power of a mobile radio signal," *IEEE Trans. Veh. Technol.*, vol. 34, no. 1, pp. 22–27, Feb. 1985.

[49] A. J. Smola and B. Schölkopf, "A tutorial on support vector regression," *Statist. Comput.*, vol. 14, no. 3, pp. 199–222, Aug. 2004. [Online]. Available: https://doi.org/10.1023/B:STCO.0000035301.49549.88

[50] L. Breiman, "Random forests," *Mach. Learn.*, vol. 45, no. 1, pp. 5–32, 2001. [Online]. Available: http://dx.doi.org/10.1023/A%3A1010933404324

[51] A. Smola and B. Schölkopf, "A tutorial on support vector regression," *Statist. Comput.*, vol. 14, pp. 199–222, 2004.

[52] V. N. Vapnik, *The Nature of Statistical Learning Theory*. New York, NY, USA: Springer-Verlag, 1995.

[53] F. Pedregosa, G. Varoquaux, A. Gramfort, V. Michel, B. Thirion, O. Grisel, M. Blondel, P. Prettenhofer, R. Weiss, V. Dubourg, J. Vanderplas, A. Passos, D. Cournapeau, M. Brucher, M. Perrot, and E. Duchesnay, "Scikit-learn: Machine learning in Python," *J. Mach. Learn. Res.*, vol. 12, pp. 2825–2830, Oct. 2011.

[54] G. Biau, "Analysis of a random forests model," *J. Mach. Learn. Res.*, vol. 13, pp. 1063–1095, Apr. 2012.

MARCO SOUSA received the B.Sc. degree in electronic and telecommunications engineering from the Universidade da Madeira (UMa), Portugal, in 2014, and the M.Sc. degree in electronic and telecommunications from the Instituto Superior de Engenharia de Lisboa (ISEL), Portugal, in 2017. He is currently pursuing the Ph.D. degree in electrical and computer engineering (PDEEC) with the Instituto Superior Técnico (IST), Technical University of Lisbon, Portugal. Since 2015, he has been working at the Research Department of CELFINET, a Portuguese technological consultancy company. He is currently the team leader of the research activities related to mobile network configuration management and optimization. His main research interests include mobile network optimization, radio access network coverage and interference, and applied machine learning/deep learning algorithms for mobile networks.

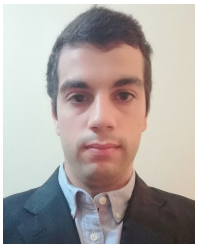

ANDRÉ ALVES received the M.Sc. degree in electrical and computer engineering from the Instituto Superior Técnico (IST), Portugal, in 2020. From 2019 to 2020, he was an Intern with the Research Department of CELFINET, a Portuguese technological consultancy company, where he worked in the fields of mobile network configuration management and optimization, mainly regarding 5G coverage prediction and optimization. Since 2020, he has been working as an RF Test and Analysis Engineer at Huawei Technologies Deutschland GmbH, a global provider of information and communications technology (ICT) infrastructure and smart devices, where he is involved in activities related to 4G and 5G network planning and optimization. His main research interests include radio access network configuration, testing, optimization, and developing smart algorithms to further automate the former.

PEDRO VIEIRA was born in Lisbon, Portugal, in 1974. He received the degree in engineering, and the M.Sc. and Ph.D. degrees in electrical and computer engineering from the Instituto Superior Técnico (IST), Technical University of Lisbon, Portugal, in 1997, 2003, and 2008, respectively. Since 1997, he has been with the Department of Electronics, Telecommunications and Computer Engineering, Lisbon Polytechnic Institute (ISEL). He is currently an Adjunct Professor with ISEL and a Researcher at the Instituto de Telecomunicações, where he is researching aspects of wireless communications, including radio propagation, radio network planning, and optimization and SON systems. He is also a Senior Engineer registered at the Portuguese Engineering Order (OE), and an OE telecommunications specialist, since 2008. He is leading the research activities at CELFINET, a Portuguese technological consultancy company, where he is engaging in applied research to create new methodologies, tools, and algorithms for the mobile communications business.

MARIA PAULA QUELUZ received the B.S. and M.S. degrees in electrical and computer engineering from the Instituto Superior Técnico (IST), University of Lisbon, Portugal, and the Ph.D. degree from the Catholic University of Louvain, Louvain-la-Neuve, Belgium. She is currently an Assistant Professor with the Department of Electrical and Computer Engineering, IST, and a Senior Research Member of the Instituto de Telecomunicações, Lisbon, Portugal. Her main scientific interests include image/video quality assessment, image/video processing, and wireless communications.

ANTÓNIO RODRIGUES (Member, IEEE) received the B.S. and M.S. degrees in electrical and computer engineering from the Instituto Superior Técnico (IST), Technical University of Lisbon, Lisbon, Portugal, in 1985 and 1989, respectively, and the Ph.D. degree from the Catholic University of Louvain, Louvain-la-Neuve, Belgium, in 1997. Since 1985, he has been with the Department of Electrical and Computer Engineering, IST, where is currently an Assistant Professor. He is also a Senior Research Member with the Instituto de Telecomunicações, Lisbon, Portugal. His current interests include mobile and satellite communications, wireless networks, modulation, and coding and multiple access techniques.